THE EFFECTS OF THE HARTMAN CAVITY ON THE PERFORMANCE OF THE USGA NOZZLE USED FOR ALUMINUM SPRAY FORMING

Adel Mansour*, Norman Chigier* Tom I-P. Shih* and R. L. Kozarek**
*Department of Mechanical Engineering
Carnegie Mellon University
Pittsburgh, PA 15213
**Aluminum Company of America

ABSTRACT

This paper addresses the effects of the Hartman cavity on the performance of the USGA (Ulrasonic Gas Atomizer) used for aluminum spray forming. Numerical simulations of the gas flow field have been performed with the aim of establishing the effects of the Hartman cavity on flow development both inside and outside the air nozzles. PDPA measurements have been made of gas velocity and turbulence intensity, droplet mean and fluctuating velocity, and droplet size across planes at various distances downstream. High speed imaging is used in the flow region near the orifice exit where recirculation zones are generated and there is concern about metal droplet deposition on atomizer surfaces. Shadowgraphic photographs show the presence of shock waves and cells in the emerging gas jets. It was found that the Hartman cavity has little effect on the droplet sizes generated. The Hartman cavity also has little effect on spray development. The rectangular slit orifices for the two gas jets and the liquid jet generate a spray, after impingement, which is somewhat rectangular in cross section. As the spray develops downstream it changes shape under the influence of entrainment from the gas surrounding the spray. After a distance of 254 mm from the nozzle exit, the width and breadth of the jet are equal but significant shape changes occur further downstream. Gaussian velocity distributions result in liquid flux distributions and metal deposits with Gaussian shapes, instead of deposits with uniform thickness.

DISCLAIMER

INTRODUCTION

Over the past several years, continuous casting of aluminum has been gaining acceptance for the production of low-alloy sheet products, replacing more conventional ingot metallurgy/hot milling processes. Spray forming is a technology based on the atomization of liquid melts and subsequent deposition on a substrate. ALCOA with support from DOE is investigating the feasibility of manufacturing aluminum sheet by direct spraying of molten aluminum onto moving substrates. In order to prevent oxidation of the aluminum, nitrogen gas is used for atomization and cooling. Atomizers need to be designed to generate sprays that will deposit aluminum droplets on the moving substrate. The deposited aluminum should have the prescribed uniform aluminum sheet thickness, temperature, porosity and other metallurgical properties. The properties of the aluminum sheet are directly dependent upon the liquid metal spray characteristics during impingement. The nitrogen gas is deflected by the moving substrate and carries small aluminum particles into the over spray. The largest droplets will impinge directly on the substrate if their momentum/drag ratio is sufficiently high. The major portion of the small droplets will be deflected by the impinging nitrogen gas stream.

In addition to eliminating several processing steps, a spray formed material is metallurgically superior to continuous cast materials because of the following characteristics:

- Uniform distribution of equiaxed grains (< 200 mm)
- No macroscopic segregation of alloying elements
- Extension of the solid solubility of the alloy
- Uniform distribution of second phases
- Improved tolerance to impurities
- Low oxide content
- Absence of powder particle boundary
- Potential for metal matrix composite

Conducting tests and experiments using molten aluminum is very expensive. A series of studies was conducted at Carnegie Mellon University using water and air to simulate the molten metal studies conducted at ALCOA. The modeling studies take into account the principal physical properties that affect atomization, the most important difference in this case is the order of magnitude increase of surface tension for aluminum compared to water. The physical modeling studies at Carnegie Mellon use the same (or similar) geometry for the liquid and gas passage-ways in the atomizers as the ALCOA atomizers. Linear or planar nozzles have been selected because of their potential advantages of high production rates, minimization of overspray and improved flatness for wide sheet production.

The studies at Carnegie Mellon use an ALCOA designed Ultrasonic Gas Atomizer (USGA). Figure 1 shows a schematic of the deposition setup along with the USGA nozzle. The USGA nozzle provides an example of the confined-liquid gas atomizer, in which the metal delivery tube is situated in close proximity to the high velocity gas jets. Aerodynamic interaction between the emerging gas jets and the face of the nozzle result in formation of strong recirculation zones with associated sub-ambient pressures that pull the liquid metal out of the nozzle at velocities higher than the liquid metal free fall velocity [1]. The liquid metal spray is formed after the impingement of two high speed linear gas jets on the liquid sheet. In this linear nozzle design the gas jets emerge from rectangular slits placed on either side of the confined metal nozzle. An integral part of the design is the use of the Hartman shock tubes which are claimed to provide ultrasonic energy to the melt, aiding atomization. Figure 2 shows the details of the air nozzles. Note that in Fig. 2 one of the nozzles is drawn with the Hartman cavity and the other without. The coordinate system utilized is also shown in Fig. 2. x is the axial distance downstream from the liquid nozzle; y is the distance along the liquid metal slit starting at the slit center and z is the lateral distance perpendicular to the slit, starting at the slit center. This paper addresses the effects of the Hartman cavity on the atomization of the liquid sheet. Numerical simulations of the gas flow field have been performed

with the aim of establishing the effects of the Hartman cavity on flow development both inside and outside the air nozzles. PDPA measurements were made of gas velocity and turbulence intensity, droplet mean and fluctuating velocity, and droplet size across planes at various distances downstream. High speed imaging is used in the flow region near the orifice exit where recirculation zones are generated and there is concern about metal droplet deposition on atomizer surfaces. Shadowgraphic photographs show the presence of shock waves and cells in the emerging gas jets. Using LDV, detailed measurements have been made of velocity distributions in the gas jets emerging at sonic speeds from the nozzle exits.

EXPERIMENTAL PROCEDURE

Three air nozzles configurations were supplied by ALCOA for testing. Two of the air nozzles had a slit length of 25.4 mm and a slit width of 0.508 mm. The only difference between these two nozzles is that one of the nozzles was equipped with a Hartman cavity and the second was without the cavity. The third air nozzle had a slit length of 101.6 mm and a slit width of 0.508 mm. Two liquid nozzle were also supplied by ALCOA for study of spray characteristics. One had a slit length of 25.4 mm. This nozzle was operated with the two 25.4 mm air nozzles described above. The other liquid nozzle had a slit length of 76.2 mm and was operated with the 101.6 mm air nozzle described above. Thus, there was an overlap on 12.7 mm on either side of the liquid nozzle. Both liquid nozzles had a slit width of 0.508 mm. The air nozzle impingement angle was set at 10 degrees for all nozzles.

An analysis has been made of the flow conditions in the air nozzles by applying isentropic flow assumptions. The theoretical air mass flow rate can be expressed in terms of air properties at the nozzle exit [2].

$$\frac{m_{th}}{A} = P_1 M_1 \sqrt{\frac{\gamma}{RT_1}} \qquad (1)$$

in which A represents the nozzle exit area, and the nozzle exit Mach number, M_1, is given for a perfect gas by

$$M_1 = \sqrt{\left\langle \left(\frac{P_0}{P_1}\right)^{\frac{\gamma-1}{\gamma}} - 1 \right\rangle \left(\frac{2}{\gamma-1}\right)} \qquad (2)$$

where P_o denotes stagnation pressure and the subscript "1" refers to properties at the nozzle exit. For air the specific heat ratio is $\gamma = 1.4$ and the gas constant $R = 287$ J/kg K. The variations of the specific air mas flux m_{th}/A and the nozzle exit mach number M_1 are plotted as a function of stagnation pressure P_o in Fig. 3. Based on isentropic flow assumptions, the stagnation pressure P_{oc}, at which flow choking is initiated, was calculated to be 191.5 kPa. With a further increase in stagnation pressure the exit Mach number remains unity but the air density increases progressively due to compression, and thus the air mass flux continues to increase.

The discharge coefficient for all three air nozzle was determined. The actual air mass flow rate m_a was measured using the Air Products vortex flow meter. The discharge coefficients for air nozzles are determined from the expression, $C_d = m_a/m_{th}$, where m_a is the actual mass flow rate and m_{th} is the mass flow rate determined from the stagnation pressure (P_o) and the stagnation temperature (T_o) by means of isentropic flow assumptions. The discharge coefficient is an indication of frictional losses inside the nozzle. Boundary layers that develop and grow along solid walls result in the reduction of the discharge coefficient from an ideal value of 1, which corresponds to the case when the fluid is frictionless. The calculated values of the discharge coefficients are in the range of 0.8 to 0.96 with the 101.6 mm nozzle yielding lower discharge coefficients (see Fig. 4). These values of the discharge coefficient compare well with those reported by Mansour et al. [3] for two-dimensional (linear) nozzles. Figure 4 shows that the discharge coefficient increases with increasing stagnation pressure. The most important factor that results in the reduction of the actual mass flow rate below the isentropic value is the presence of friction in real fluids as a result of boundary layer development along solid walls. As a result of

increase in the stagnation pressure, the boundary layer displacement thickness decreases [4]. The boundary layer displacement thickness is proportional to an inverse power of the Reynolds number for both laminar and turbulent conditions. The decrease in the displacement thickness as the stagnation pressure is increased can be explained as follows: As P_o is increased beyond choked conditions, gas density at the throat is increased (in linear proportion) while gas temperature and gas velocity (sonic at the throat) remain the same. Thus the overall effect of increasing P_o is to increase the Reynolds number under otherwise identical conditions. The reduction in the boundary layer displacement thickness results in the reduction of frictional losses and thus to the increase of the discharge coefficient.

Figure 4 also shows the discharge coefficient of the air nozzle which is equipped with the Hartman cavity. The discharge coefficient for the Hartman cavity nozzle is observed to be slightly smaller than that of the nozzle devoid of the Hartman cavity. These differences can arise because of two primary reasons. First the presence of the Hartman cavity can result in added frictional losses. Second, small variations in the exit areas of the two nozzles can result in the observed discrepancy. Due to the very small differences in the discharge coefficient, it was not possible to ascertain which of the previously mentioned factors plays the most prominent role in the observed reduction in the discharge coefficient.

RESULTS AND DISCUSSION

NUMERICAL SIMULATION OF THE GAS FLOW IN THE USGA NOZZLE

Computations were performed to investigate the two dimensional flow in the USGA nozzle with the Hartman cavity. Though the flow in the nozzle may be unsteady, depending upon flow conditions, only steady-state solutions were considered. In the computations, the governing equations used are the conservation of mass, momentum (compressible Navier-Stokes), and total energy. The grid system used is shown in Fig. 5. It involves four blocks of boundary conforming

structured grids with a total of about 120,000 grid points. Since only steady solutions are sought, the Euler implicit formula was used for all time derivatives. All spatial derivatives were replaced by central differencing formulas. Since central differencing of inviscid flux-vector terms causes numerical instability, a blended second and fourth order artificial dissipation was added. Solutions to the resulting nonlinear system of equations were obtained by using a diagonalized alternating implicit scheme. Some typical solutions generated in and around the Hartman nozzle are shown in Figs. 6 to 8. Figure 6 shows the velocity vectors and streamlines inside the Hartman nozzle. This figure also shows a streamwise separation bubble at the edge of the 90-degree bend which effectively creates a converging diverging nozzle in the straight section downstream of the cavities. Figure 7 shows the velocity vectors and streamlines at the exit of the Hartman nozzle. The high velocity at the exit produced very low static pressures which induced flow towards the nozzle face from the rest of the domain. Figure 8 shows the Mach number contours in and around the Hartman nozzle. From these figures, it can be seen that the flow can be slightly supersonic inside the exit channel. At the exit of the nozzle, the diffuser like streamlines further accelerate the flow. Also, complex reflected oblique shock structures form.

FLOW AND SPRAY VISUALIZATION

Photographic Visualization of Spray

Microphotography was used to determine the global structure of the sprays. Instantaneous flow field images were obtained with a Canon F1 camera with a f = 200 mm macro lens. An Electro-Optics EG&G microflash was used to provide a 0.5μs flash duration and 5×10^7 beam candlepower light intensity. At low air stagnation pressures (108.25 kPa) it was seen that the liquid sheet develops waves which grow in the downstream direction from the nozzle exit. These waves shed ligaments which rapidly contract under the action of surface tension to form droplets [5]. At an air pressure of 135.83 kPa, a local low pressure zone is formed around the liquid nozzle face.

This has the effect of drawing small amounts of liquid from the liquid sheet along the face of the liquid nozzle. The local low pressure zone is shown clearly in Fig. 7. With a further increase of the stagnation pressure, the strength of this recirculation zone is increased and the amount of liquid drawn along the liquid nozzle face increased. Figure 9 shows an artist's sketch of the effects of the low pressure zone on the liquid flow. Although an appreciable amount of liquid is drawn along the face due to the presence of the low pressure zone, photographs of the spray have shown that the majority of liquid is not affected by the presence of the recirculation zone and the liquid continues to flow undeflected from its original flow direction (i.e., the Z-direction).

Photographs were also taken of the spray impinging on a plate located at an axial position x = 254 mm downstream from the nozzle exit and centered around the spray centerline. These photographs show that a large amount of liquid is rebounded in the form of secondary droplets that are formed after shattering of the incoming primary droplets on the substrate (see Fig. 10). There is evidence to show that the rebounding distance or height decreases with increase in air stagnation pressure. This is due to two primary reasons. First, with increase in stagnation pressure, the flow velocity opposing the rebounding droplets increases. Second, increases in air stagnation pressure result in generation of smaller droplets with lower momentum that are more prone to follow the air streamlines.

Shadowgraphic Visualization of Air jets

The optical arrangement for the Shadowgraphic technique is shown schematically in Fig. 11. A metal-halide arc lamp fitted with an aperture was used to generate a point light source. Light intensity variations in the Shadowgraphic technique are sensitive to changes in the second derivative of density or refractive index of the medium [6]. Figures 12, 13 and 14 show typical shadowgraphs of shock wave patterns for the air jets when the nozzle is operated at stagnation pressure of 200, 218 and 356 kPa, respectively. The right nozzle in these figures had the Hartman

cavity and the left nozzle was without the cavity. For the nearly adapted jets (P_o = 200 kPa), no shock waves have been identified and the slightly underexpanded jets diffuse according to viscous dissipation. As the stagnation pressure is increased, shock cell structures become clearly visible and the size and strength of individual cells increase. The shock wave patterns eventually diffuse away in the downstream region from the nozzle exit. The flow converts to subsonic free jets with growth of mixing layers downstream. The light intensity variations shown in the shadowgraphs are attributed to the spatial distribution of the ratio of the local to the ambient air density. The Mach number in each jet periodically varies along the shock cell and ranges from sonic to supersonic when the jets are underexpanded. It is interesting to note that the shock cells of the nozzle which is equipped with the Hartman cavity are much more well defined than that without the cavity. These effects should in principle result in better atomization characteristics for the nozzles with the Hartman cavity; nozzles with the Hartman cavity are able to create and sustain supersonic gas jets to lengths that far exceed those that can be created with nozzles without the cavity. Thus, from these photographs it can be concluded that the Hartman cavity focuses the air jets downstream from the nozzle thereby reducing the initial spreading of the jets. These effects can be seen more clearly in Fig. 14.

PHASE DOPPLER INVESTIGATION OF SPRAY

The Phase Doppler (PDPA) light scattering technique developed by Bachalo and Houser [7] for spray analysis was used to make measurements of joint droplet size-velocity distribution functions in the sprays. These measurements are made in situ and non-intrusively which is important when measuring easily deformable particles or probing turbulent flow fields. The PDPA instrument is an extension of the laser Doppler velocimeter. The PDPA provides many useful parameters for spray characterization including temporal and spatial mean drop size, local drop size distribution, drop velocity, volume flux, and number density. The optical system was configured with a 300 mm focal length collimating lens and 495 mm focal length transmitting lens. The

receiver was placed 30 degrees off axis in the forward scatter mode and was fitted with a 50 μm aperture. Since the PDPA available to us is limited to a dynamic range of 35 to 1, the window of drop size range must be carefully selected for multisize sprays. For the present study and depending on the spatial location of the measurements we chose size ranges that span 2.9 - 100 μm, 3.7 - 130 μm, 5 -175 μm and 6.3 - 220 μm. The smallest of the size ranges was generally chosen for measurement along the centerline and the largest size range was used for measurements around spray edges. At intermediate locations between the spray centerline and the spray edges, intermediate size ranges were used. This was chosen as a compromise between the need to measure the small droplets (<10 μm) population and the need to measure the large droplets, which carry most of the liquid mass injected. For most of the measurements, the beam diameters at the probe volume were fixed at 176 μm ($1/e^2$) and a 17.4 μm fringe spacing was used. Signals from a minimum of 16000 drops were collected at most measurement locations. Particulate acceptance rates were generally 90 % or higher. In the central portion of the spray 2 to 3 seconds sampling time was required to collect 16000 samples. Around the spray edges the time required to collect 16000 samples could extend up to 100 seconds. Generally, around the spray edges, 2000 to 5000 samples were found to be sufficient to guarantee nearly perfectly repeatable drop size and velocity distributions and mean quantity data. Experimental uncertainties were largely due to finite sampling times and flow unsteadiness. They were less than 3% for the mean velocity, 5% for the axial rms and 2 to 5% for the droplet size. These experimental uncertainties were derived from repeated attempts to measure the same quantity on different occasions. The highest uncertainties for the droplet size measurements were in locations close to the nozzle exit, where the droplet number density was highest and the probability of finding more than one droplet in the probe volume increased.

Effects of the Hartman Cavity

Two nozzles were considered for this study. The first one had a Hartman cavity and the second one was without the cavity. Both nozzles had a slit length of 25.4 mm and a slit width of 0.5 mm. The water nozzle had a slit length of 25.4 mm and a slit thickness of 0.5 mm. The water mass flow rate was kept constant at 26.67 g/s.

Effects of the Hartman Cavity on the Mean and RMS Velocity

Figure 15 shows the effects of stagnation pressure on mean and rms drop velocities measured at spatial location x = 254 mm, y = 0 mm, and z = 0 mm. The water mass flow rate was kept constant at m_l = 26.67 g/s. This figure confirms the trend that was observed previously in Fig. 4. The Hartman cavity results in small reductions in the centerline velocity. Figure 16 shows the effect of Hartman cavity on mean and rms velocity profiles measured at spatial locations x = 254 mm, y = 0 mm, with z being variable. The air stagnation pressure was kept constant at P_o = 239.26 kPa, corresponding to choked flow at the nozzle exit. Figure 16 shows that the Hartman cavity has little or no effect on velocity profile development. The discrepancies observed are due to experimental errors in setting the air impingement angles and in measuring the air and water flow rates.

Effects of the Hartman Cavity on Droplet Size

Figure 17 shows the effects of stagnation pressure on the Sauter mean diameter measured at spatial location x = 254 mm, y = 0 mm, and z = 0 mm. The water mass flow rate was kept constant at m_l = 26.67 g/s. Figure 17 shows that, for the same nozzle stagnation pressure, the Hartman cavity results in a slight increase of the Sauter mean diameter. Other diameters, including the arithmetic mean, the area mean and the volume mean diameters also show the same general trends. From Figs. 13 and 14 it was concluded that nozzles equipped with the Hartman cavity are able to sustain supersonic gas jets to lengths beyond those sustained with nozzles without the cavity. The point of impingement between the air jets and the liquid sheet occurs at spatial locations

downstream from the shock cell structures. At the impingement point the air jet velocity has decayed considerably and thus the beneficial effects of the Hartman cavity in focusing the air jets do not affect the atomization.

Figure 17 also shows that, as expected, the droplet size decreases as the stagnation pressure increases. Note however that there is a limit to the effectiveness of increasing the gas pressure, beyond which any additional increases result in very little decrease in droplet size. Atomization characteristics are a strong function of flow velocities past the liquid sheet with the air mass flow rate (or the air liquid mass ratio) playing only a secondary role at these conditions. The leveling off of the SMD with increases in pressure beyond 250 kPa is due to the fact that at these conditions any additional air flow does not necessarily come into close contact with the liquid sheet to aid atomization.

Figure 18 shows the effect of the Hartman cavity on the Sauter mean diameter profiles measured at spatial locations x = 254 mm, y = 0 mm, with z being variable. The air stagnation pressure was kept constant at P_o = 239.26 kPa, corresponding to choked flow at the nozzle exit, and the water mass flow rate was 26.67 g/s. Figure 18 shows that the Hartman cavity has little or no effect on droplet size distributions.

Air Flow Field and Spray Development

For this study the 101.6 mm air nozzles and the 76.2 mm liquid nozzle were used. The dimensions refer to nozzle slit length. Thus, there was an overlap of 12.7 mm on either side of the liquid nozzle. The air nozzles were equipped with the Harman cavity. Both the air and the liquid nozzles had a slit width of 0.508 mm. The air nozzle impingement angle was set to 10 degrees.

The air flow field was mapped without the spray in order to establish the manner in which the air velocity profiles develop. The air stagnation pressure was kept constant at P_o = 239.26 kPa,

corresponding to choked conditions at the nozzle exit. Figure 19 shows the Y-direction velocity profile as a function of downstream distance from the nozzle exit. It is seen that the air velocity decays from a maximum at the nozzle exit (sonic velocity) to 80 m/s in the first 76 mm of expansion downstream from the nozzle. The air velocity profiles develop from flat velocity profile at the nozzle exit to an inverted-U curve within the first 76 mm of expansion. At x = 254 mm, the Y-direction velocity profile approximates a Gaussian error curve.

The Z-direction velocity profiles are shown in Fig. 20. Air entrainment from the sides of the planar jets results in the decay of velocity along the centerline and the spreading of the combined jet. Z-direction jet spreading is more pronounced than Y-direction spreading due to larger entrainment from the sides of the jet. At x = 254 mm, both the Z and Y-direction velocity profiles are identical (see Fig. 21). The data of Fig. 21 confirms the trends that were observed by Trentecoste et al. [8]. Trentecoste et al have found that jets emanating from rectangular nozzles become axisymmetric at a distance of 3.5 times the nozzle slit length downstream from the nozzle exit. Figure 21 shows that USGA nozzle flow becomes axisymmertic at a distance of 254 mm, corresponding to 2.5 time the nozzle slit length. The discrepancy between the current data and that of Trentecoste et al. is due to the fact that the USGA jet is formed by the interaction of two jets impinging at an angle of 20 degrees. Further downstream the jet becomes larger in the short axis of the nozzle (i.e., the Z-axis).

Figures 22 and 23 show the mean and rms velocity distributions along the Y and Z-directions respectively, at an axial location x = 254 mm, for an air stagnation pressure of 239.26 kPa and a liquid flow rate of 88.4 g/s. These figures show that at x = 254 mm, the spray has completely lost its two dimensional character. Superimposed on these figures are the velocity profiles of the air jets when no spray is present (i.e., the liquid flow rate is zero). It is seen that the spray droplets result in the widening of the air jets particularly in the z-direction. In the central portion, the measured mean and rms velocities are larger for the air jets than the droplet laden spray. Around the edges,

the opposite is true. Around the edges, the local air velocities are nearly zero and thus small seeding droplets relax to zero velocity at these locations. Spray droplets are larger than seeding droplets and thus are able to maintain their momentum much more effectively. Around the spray edges, large droplets also show smaller rms velocities because of their longer particle response times.

The droplet size distributions along the Y and Z-directions are shown in Figs. 24 and 25 respectively. Figure 24 shows that the droplet size decreases from a maximum at the spray centerline towards the spray edges. Locally, around the spray edges, the local air/liquid mass ratio is highest due to the overlap of the liquid sheet by the air jets (i.e., liquid nozzle length = 76.2 mm, air nozzles length = 101.6 mm); this results in the observed reduction of droplet size around the spray edges. The Z- direction size profiles, shown in Fig. 25, show the opposite trends. Some of the large droplets formed after primary breakup of the liquid sheet escape the main air flow field without secondary breakup and reposition themselves around the spray boundary. This phenomenon has implications in the characteristics of the leading and trailing edges with potential effects on porosity [1].

Comparison Between the USGA Nozzle and a Linear Nozzle Previously Studied at CMU

Figure 26 shows the 2-D nozzle studied extensively at CMU. The air jets impinge on the liquid sheet immediately at the nozzle exit. Figure 27 shows a comparison between the performance of the USGA and the 2-D research atomizer studied by Khim et al [6]. It is seen that the atomization performance of the 2-D nozzle is superior to that of the USGA nozzle. The poor performance of the USGA nozzle is primarily attributed to the fact that substantial velocity decay occurs before the two air jets impinge on the liquid sheet. More intimate contact of the air jets and

the liquid sheet, with reduced length of gas jet before impact, will lead to improved atomization characteristics.

CONCLUSIONS

The two rectangular slit orifice gas jets and the liquid jet generate a spray, after impingement, which is somewhat rectangular in cross section. As the spray develops downstream it changes shape under the influence of entrainment from the gas surrounding the spray. After a distance of 254 mm (2.5 times the nozzle slit length) from the nozzle exit, the width and breadth of the jet are equal but significant shape changes occur further downstream. Most jets and sprays tend to develop Gaussian velocity distributions and these can frequently result in liquid flux distributions and metal deposits with Gaussian shapes, instead of deposits with uniform thickness. In order to generate a uniform liquid flux during impingement, the droplet size, velocity and number density must be controlled throughout the spray. This control can be exercised mainly by atomizer geometry, liquid and gas flow rates, and metal or aerodynamic shrouds. It was also shown that the Hartman cavity has little effect on flow development and droplet size downstream from the nozzle exit. The USGA nozzle is shown to be less efficient than the two dimensional nozzle previously studied at Carnegie Mellon University. Substantial velocity decay occurs in the two air jets before interaction with the liquid sheet leading to larger droplet size.

Nomenclature

A	Cross sectional area of air nozzle [m^2].
C_d	Discharge coefficient.
g	Gravitational constant [9.81 m/s^2].
M_1	Mach number at nozzle exit.
m_a	Air mass flow rate [g/s].
m_l	Liquid mass flow rate [g/s].
P_o	Stagnation pressure for air [kPa].
P_1	Air pressure at nozzle exit [kPa].
R	Gas constant [287.07 J/kg K for air].
T_o	Air stagnation temperature [K].
T_1	Air temperature at nozzle exit [K].
γ	Specific heat ratio [1.4 for air].

References

1. Kozarek R. L., Leon, D. D., and Mansour A., "Use and Characterization of Linear Nozzles for Spray Forming", Proceedings of the European Particle Metallurgy Congress, Birmingham, UK, EPMA, Oct. 1995.

2. John, J.E.A., Gas Dynamics, Allyn and Bacon, 123-129, pp 35-54 (1969).

3. Mansour, A. and Chigier, N., "Disintegration of Liquid Sheets", Physics of Fluids A, Vol. 2, No. 5, pp. 706-719 (1990).

4. Unal, A., "Gas Flow in Atomization Nozzles"

5. Mansour A, Chigier N., Shih T., Kozarek R. L., "The Effects of the Hartman Cavity on the Performance of the USGA Nozzle Used for Aluminum Spray Forming" Proceedings of the Ninth Annual Conference of Liquid Atomization and Spray Systems (ILASS- Americas), San Francisco, CA, May, 1996.

6. Khim, K. D. and Chigier, N., "Effect of Shock Waves on Liquid Atomization", Atomization and Sprays, Vol. 1, No. 1, pp 113-136, 1991.

7. Bachalo, W.D. and Houser, M.J., "Phase Doppler Spray Analyzer for Simultaneous Measurements of Droplet Size and Velocity", Optical Eng., Vol. 23, No. 5, pp583-590, (1984).

8. Trentecoste, N., and Sforza, P., "Further Experimental Results for Three-Dimensional Free Jets", AIAA J., Vol. 5, No. 5, pp 885-891, 1967.

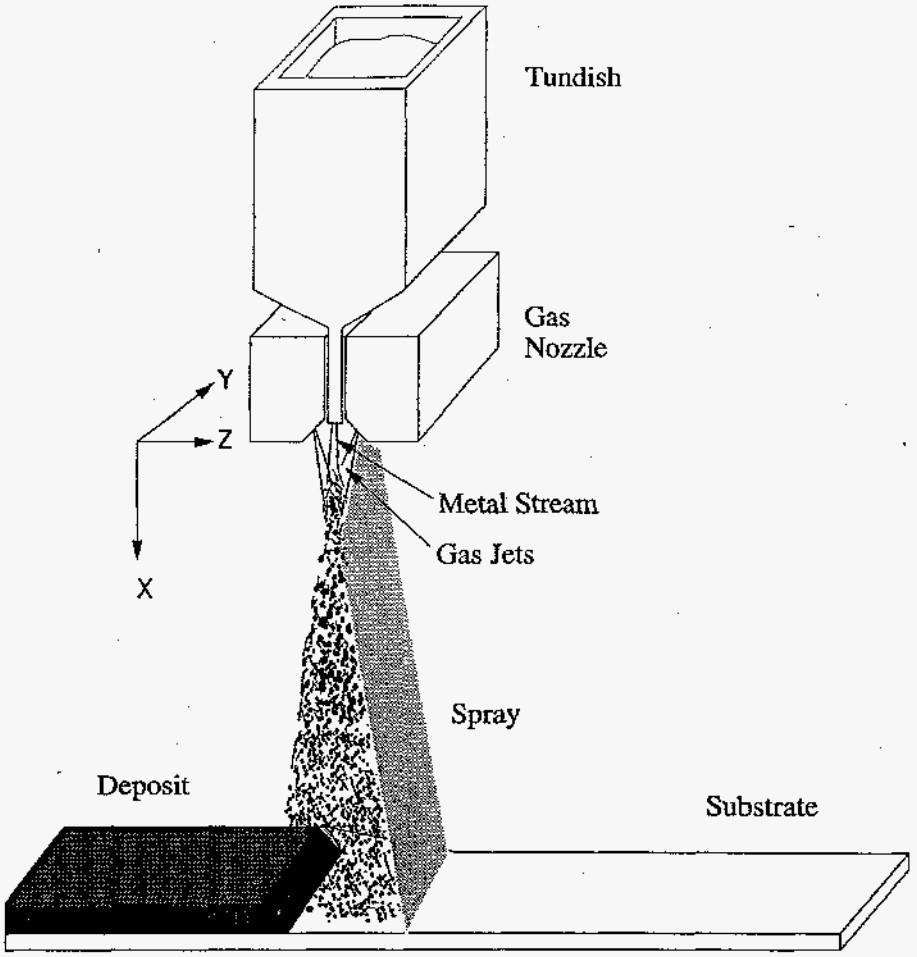

Fig. 1 Molten Metal Deposition on Moving Substrate

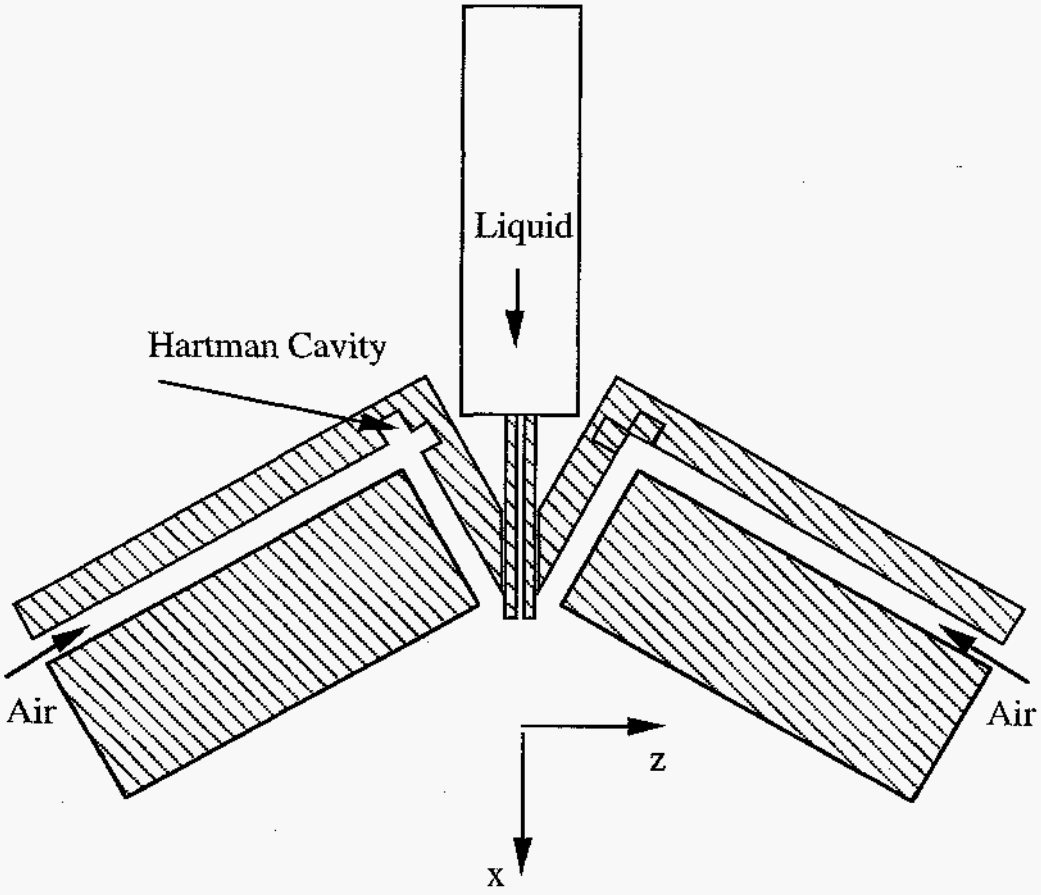

Fig. 2 The USGA Nozzle

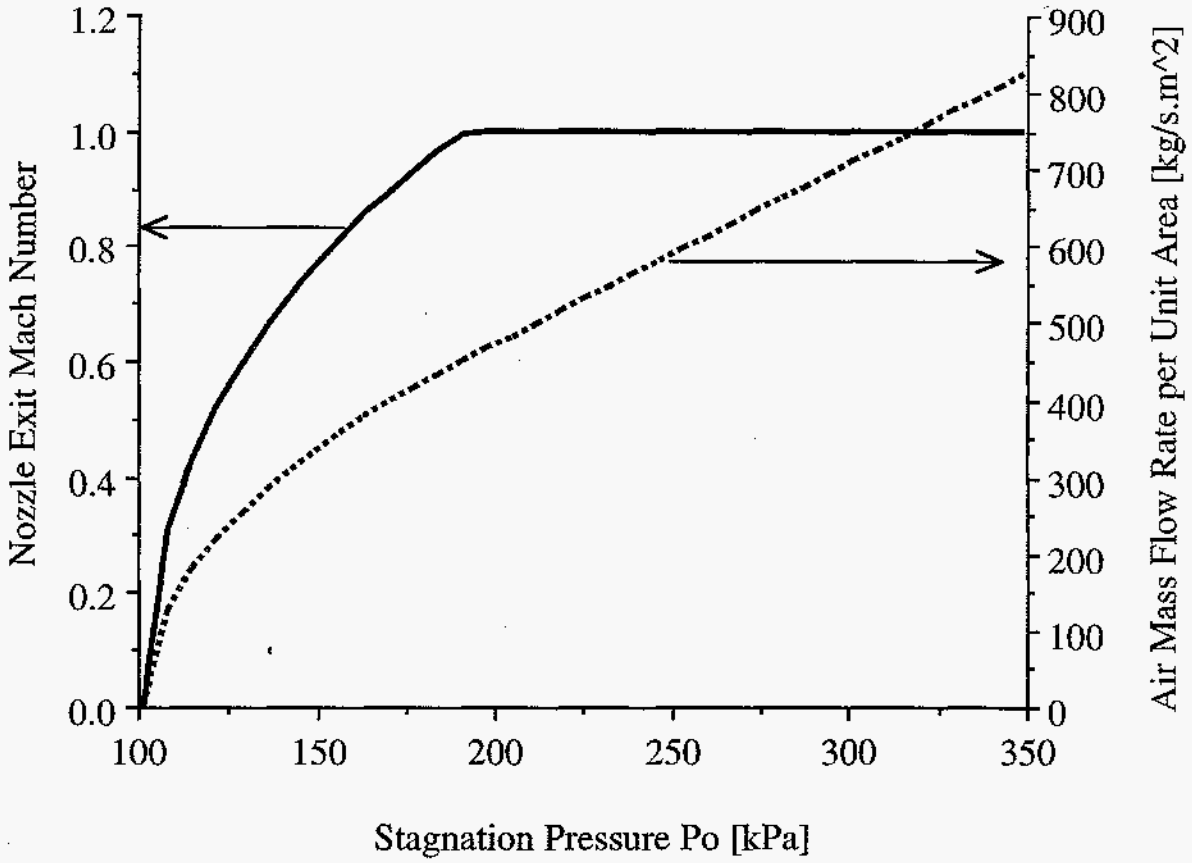

Fig. 3 Air mass flux and Nozzle exit Mach number M_1 vs. stagnation pressure P_o.

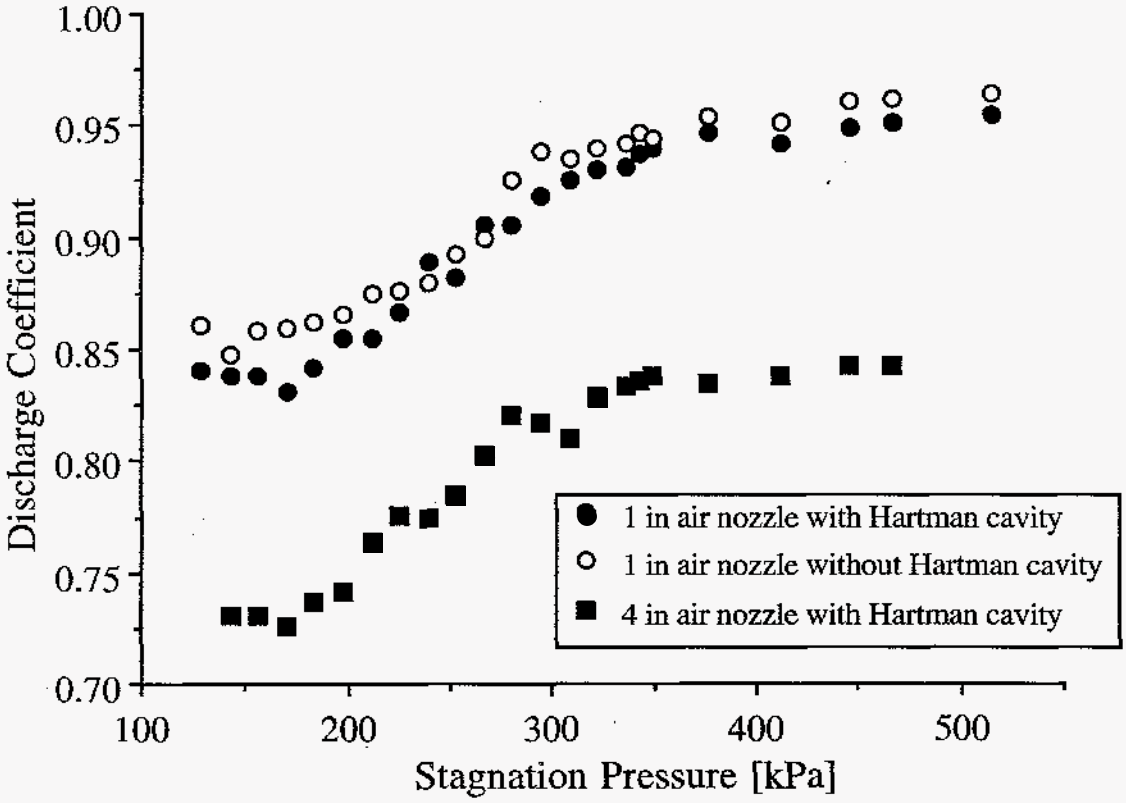

Fig. 4 Effect of Hartman Cavity on Discharge Coefficients

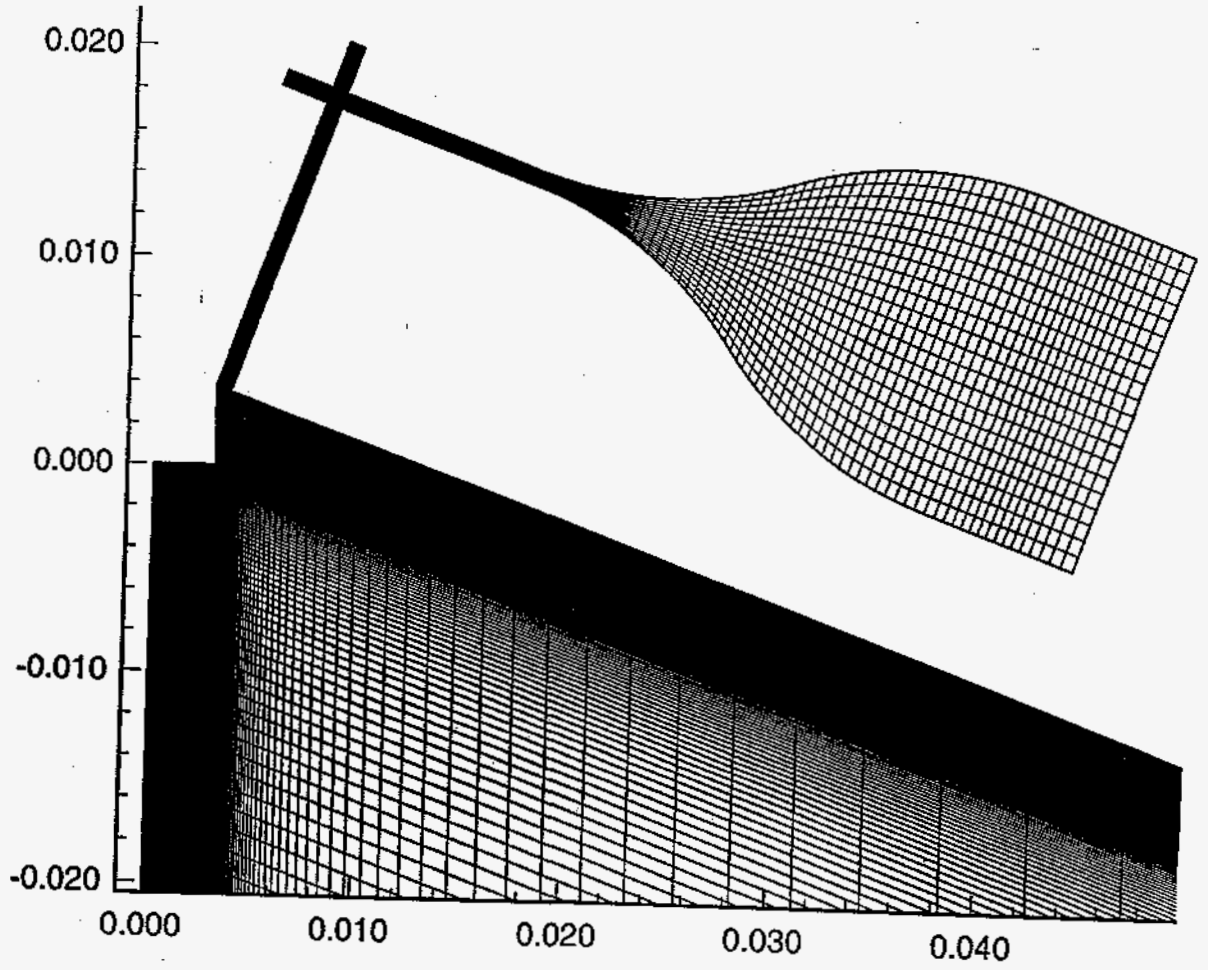

Fig. 5 The Computational Domain

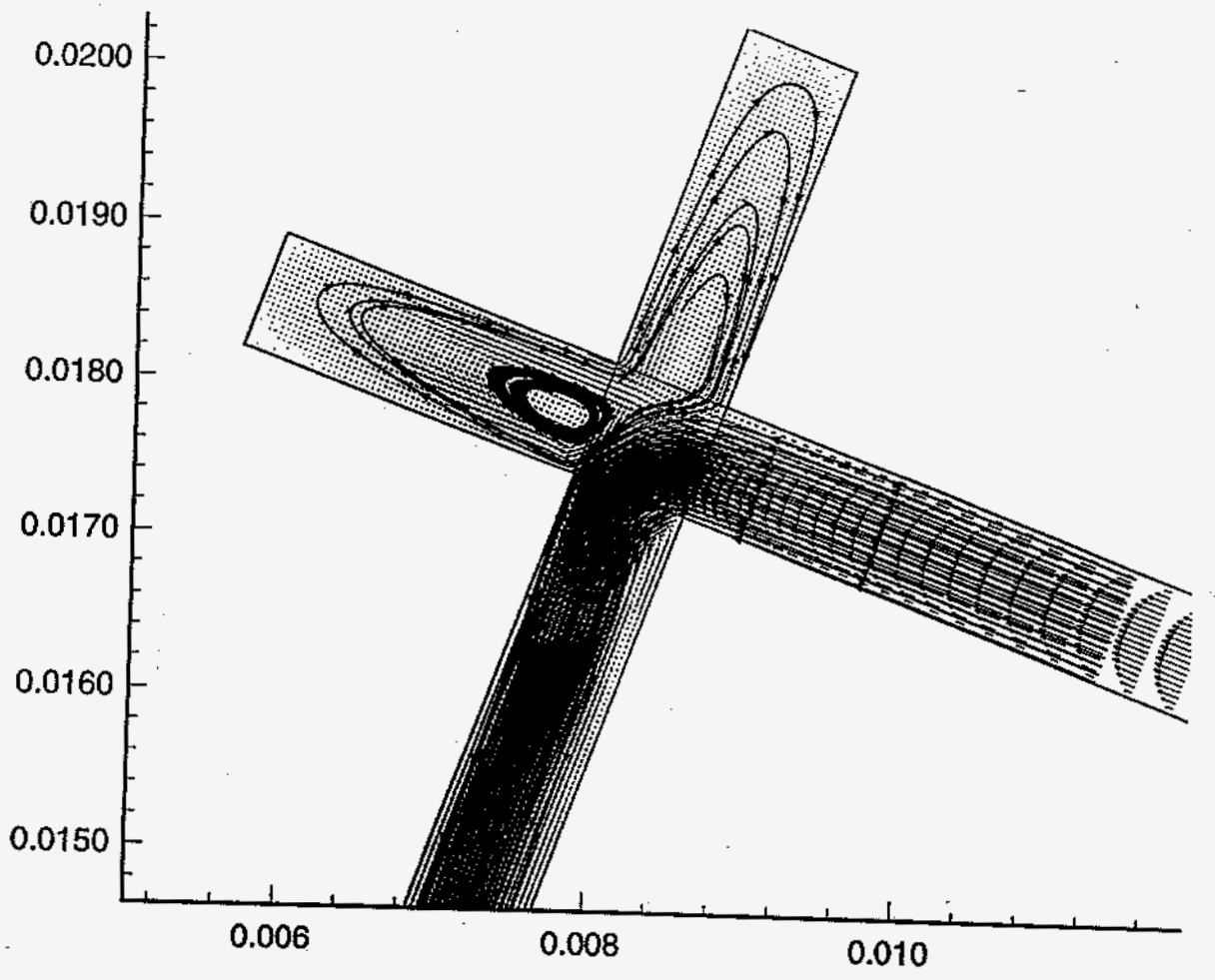

Fig. 6 Flow Field Inside the Hartman Nozzle

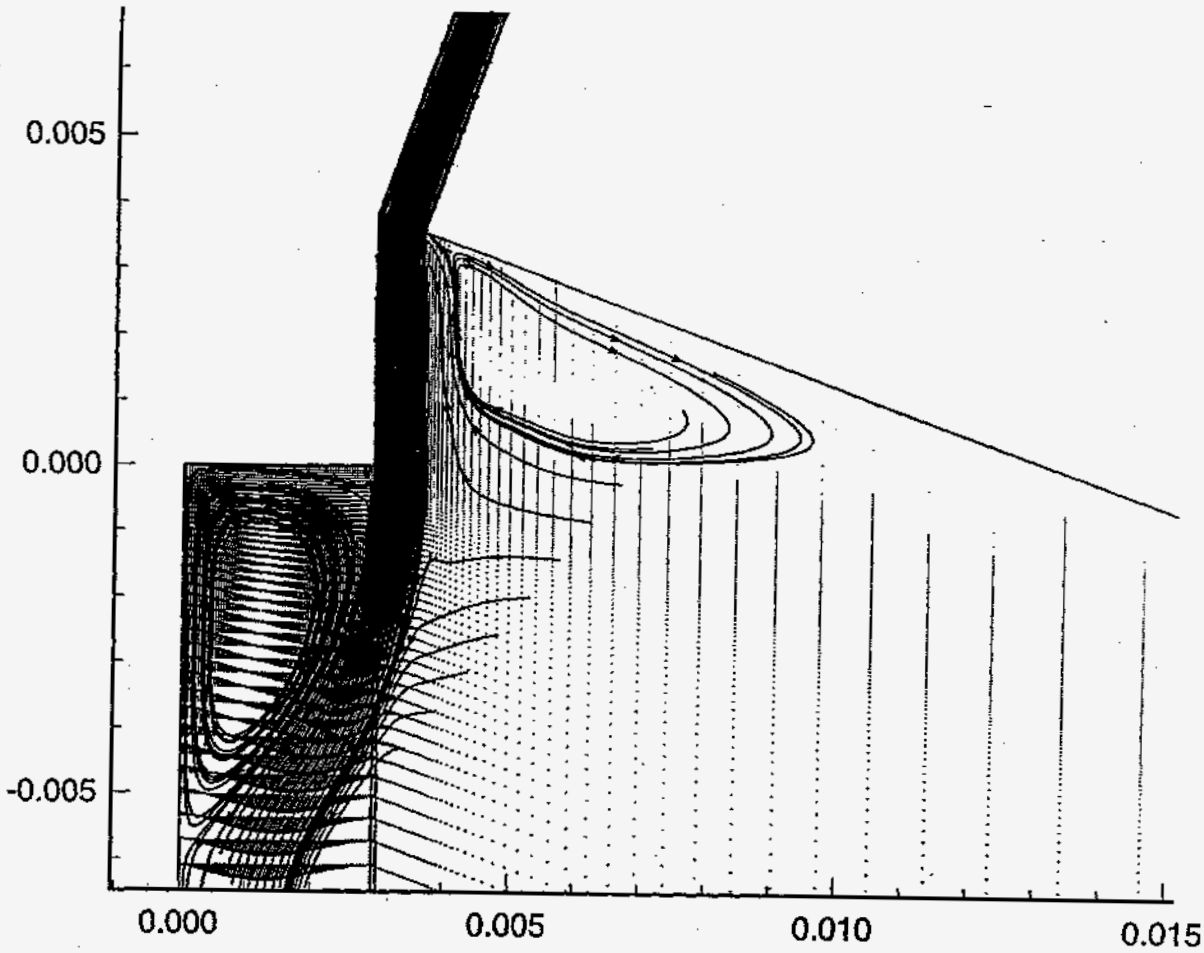

Fig. 7 Flow Field at the Exit from the Hartman Nozzle

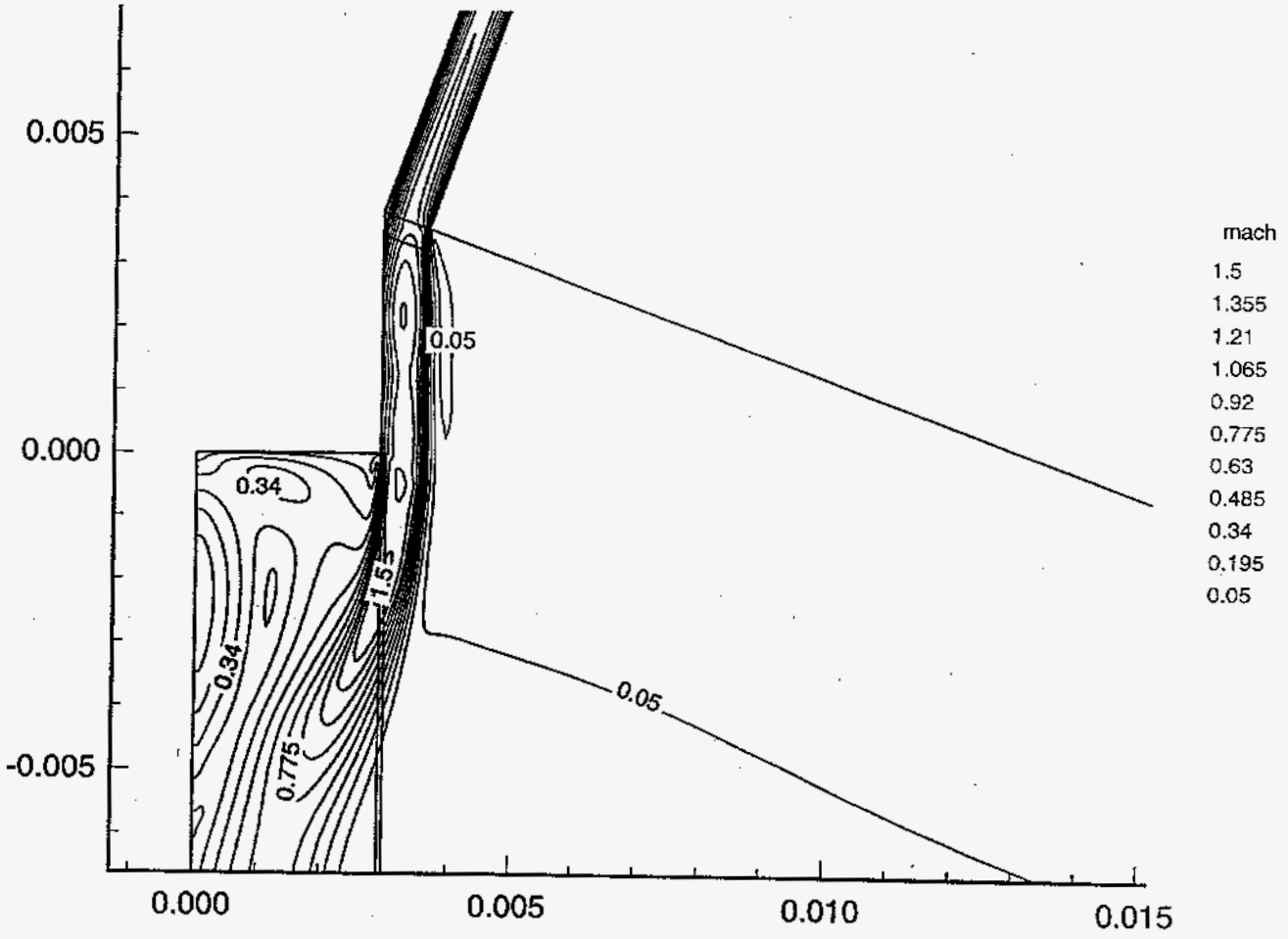

Fig. 8 Mach Number Contour

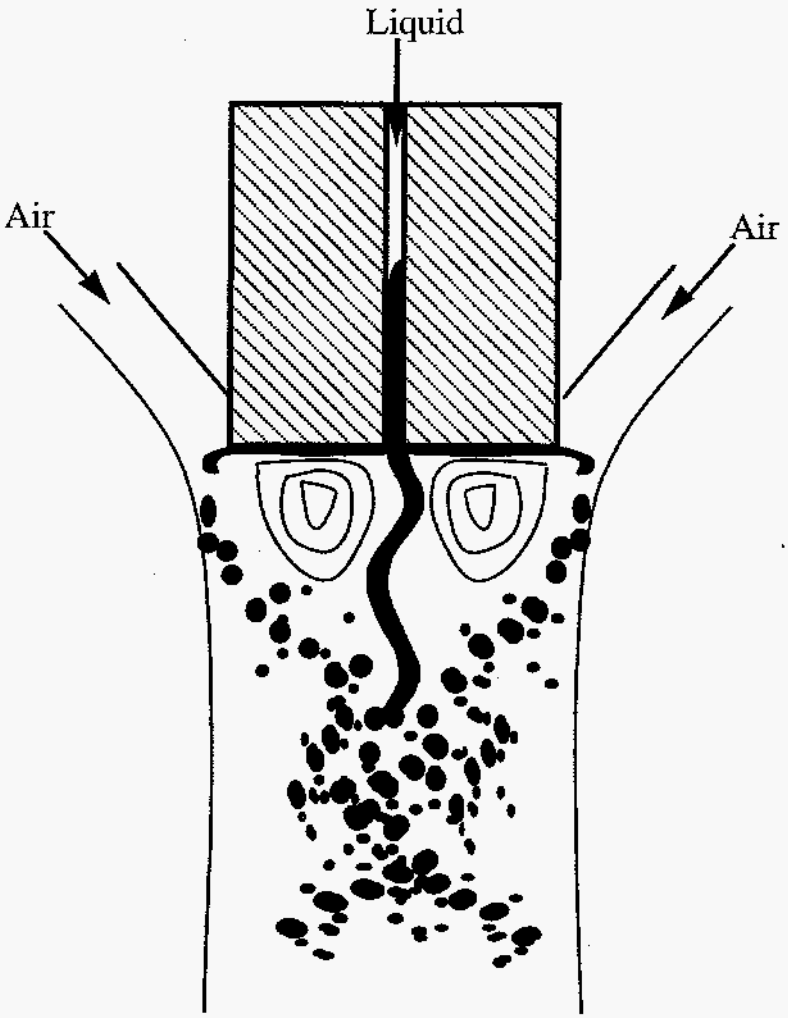

Fig. 9 Sketch of the effects of the low pressure zone on liquid flow

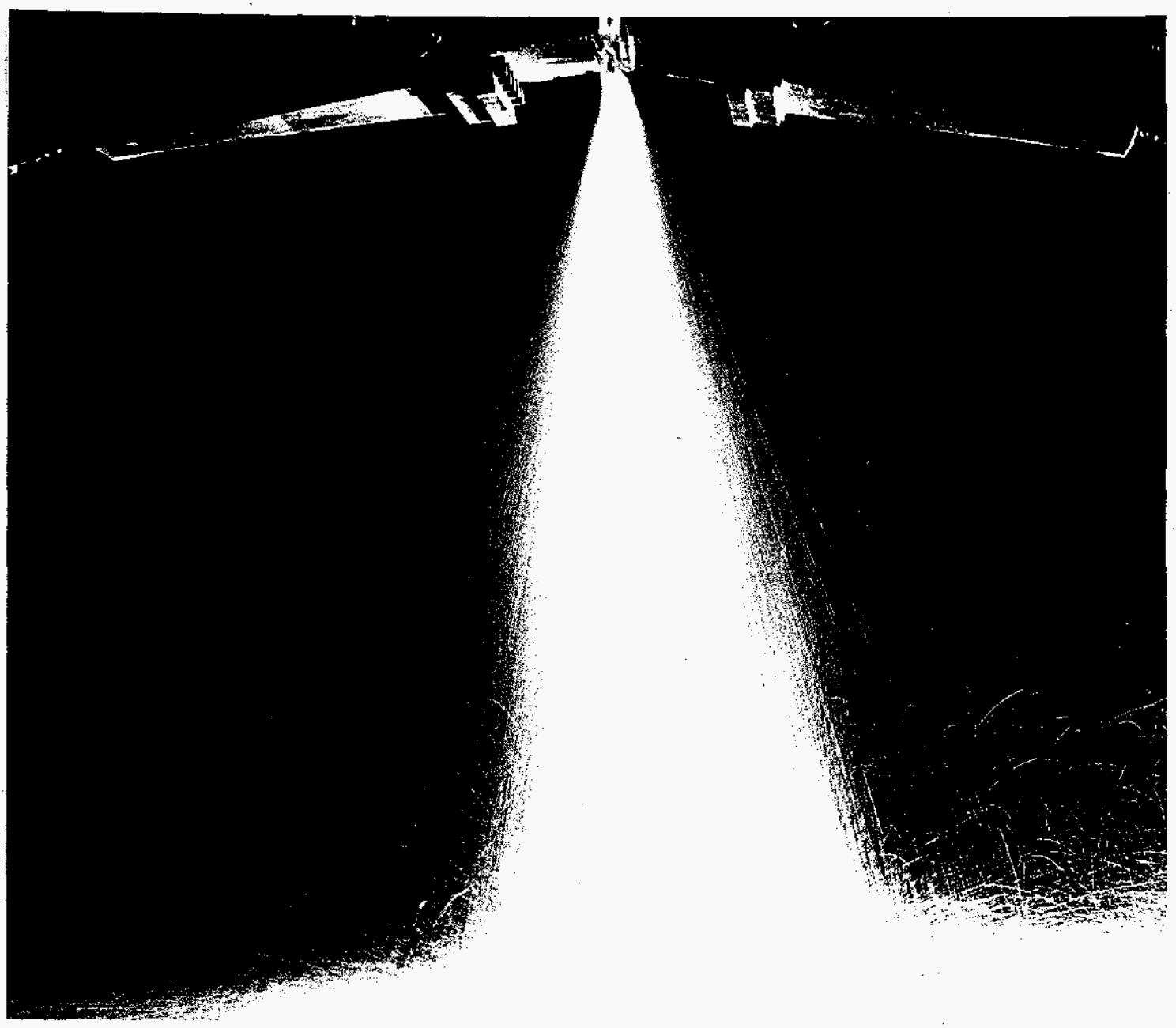

Fig. 10 Impinging Spray P_o = 135.83 kPa, m_l = 88.4 g/s.

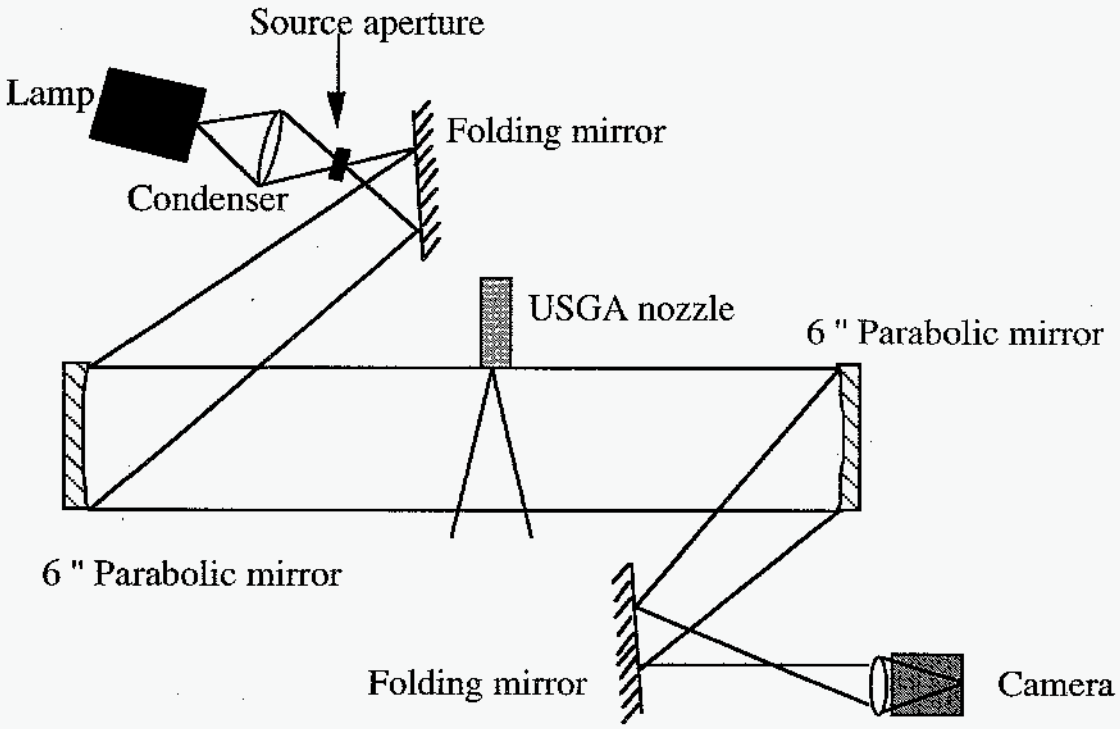

Fig. 11 Shadowgraphic system for flow visualization

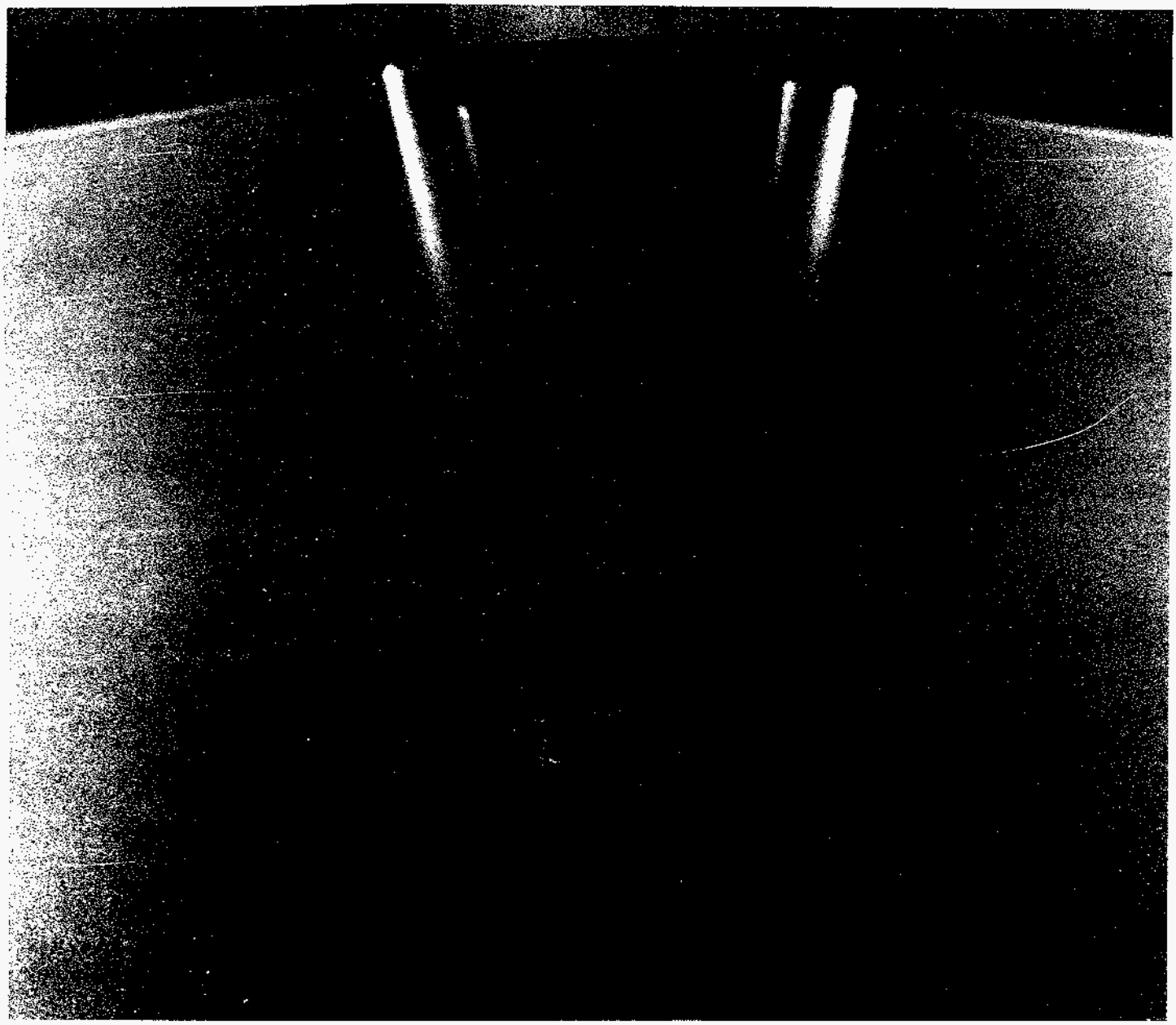

Fig. 12 Shadowgraphic visualization of air jets P_o = 200 kPa

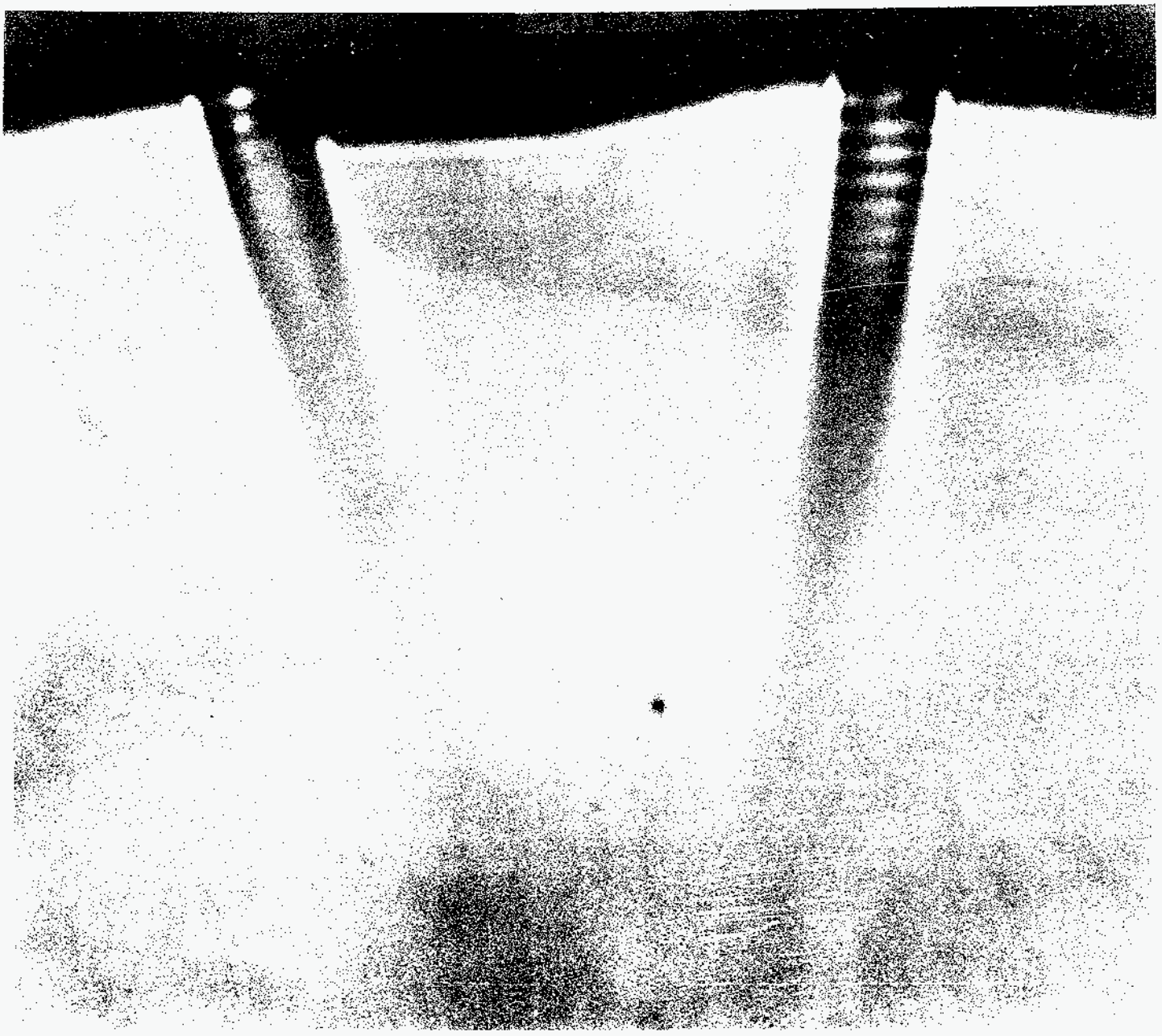

Fig. 13 Shadowgraphic visualization of air jets P_o = 218 kPa

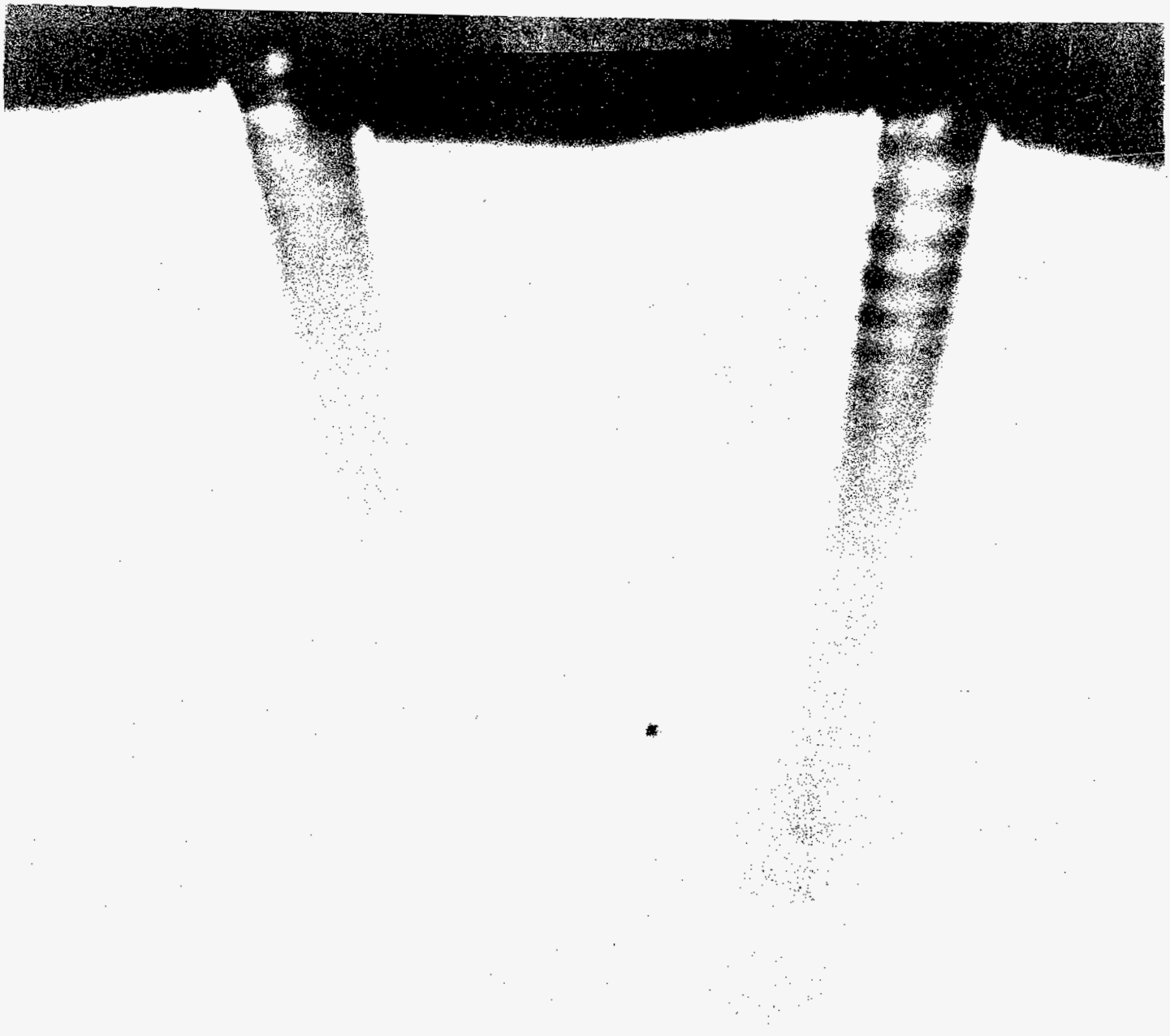

Fig. 14 Shadowgraphic visualization of air jets $P_o = 356$ kPa

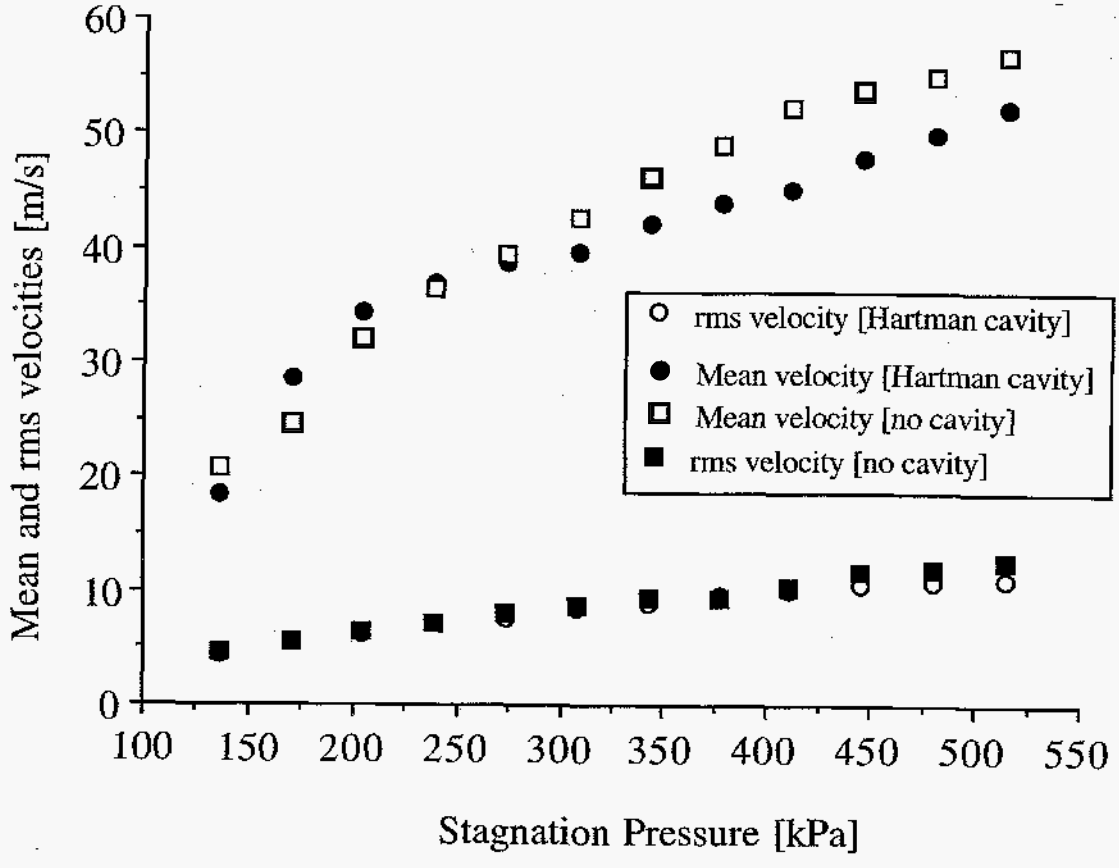

Fig. 15 Effect of Hartman Cavity on Mean and RMS Velocities at x = 254 mm, y = 0 mm, z = 0 mm, m_l = 26.67g/s.

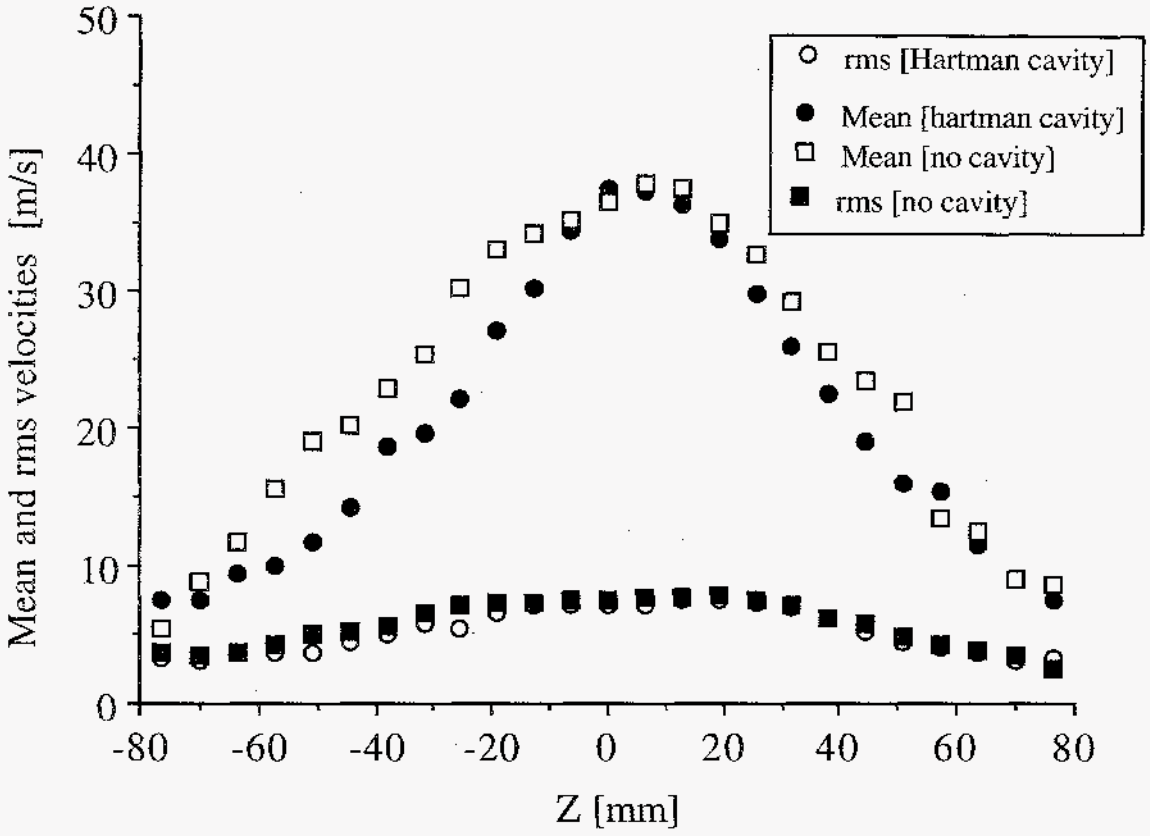

Fig. 16 Effect of Hartman Cavity on Mean and RMS Velocity Profiles at x = 254 mm, y = 0 mm, P_o = 239.26 kPa, m_l = 26.67 g/s.

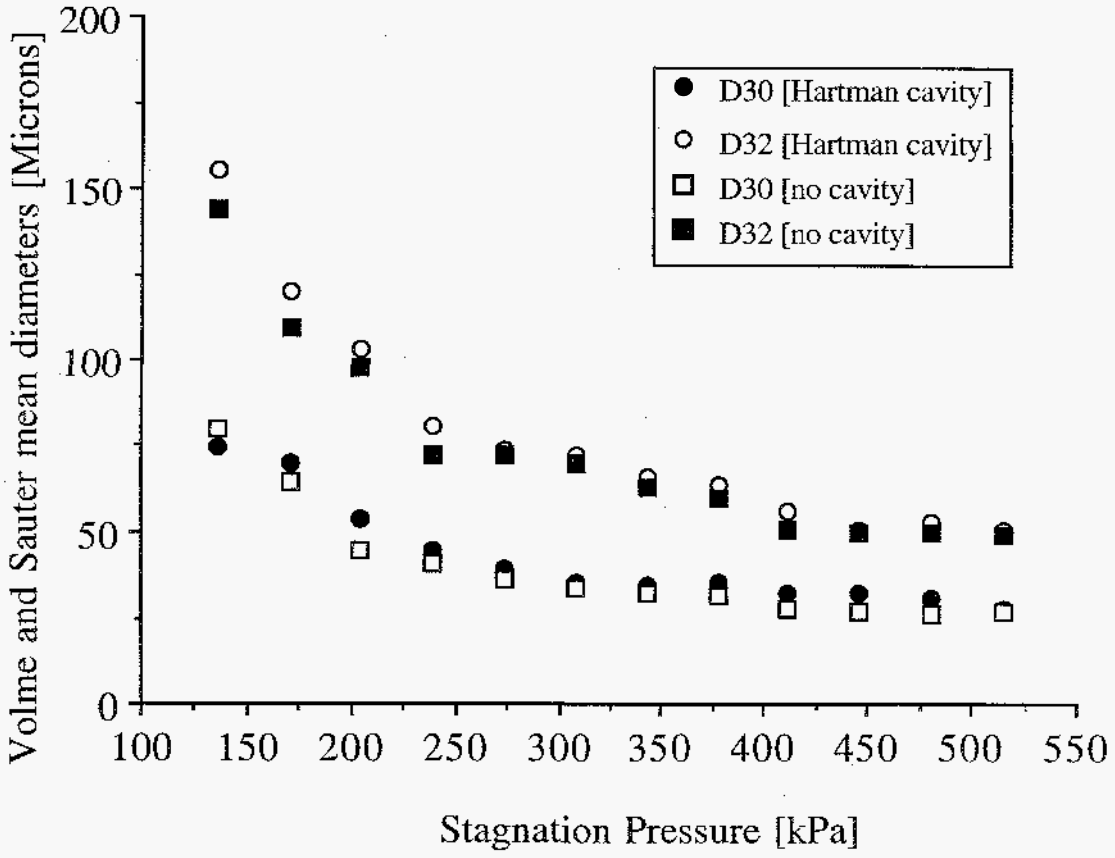

Fig. 17 Effect of Hartman Cavity on Volume Mean and Sauter Mean Diameters at x = 254 mm, y = 0 mm, z = 0 mm, m_f = 26.67 g/s.

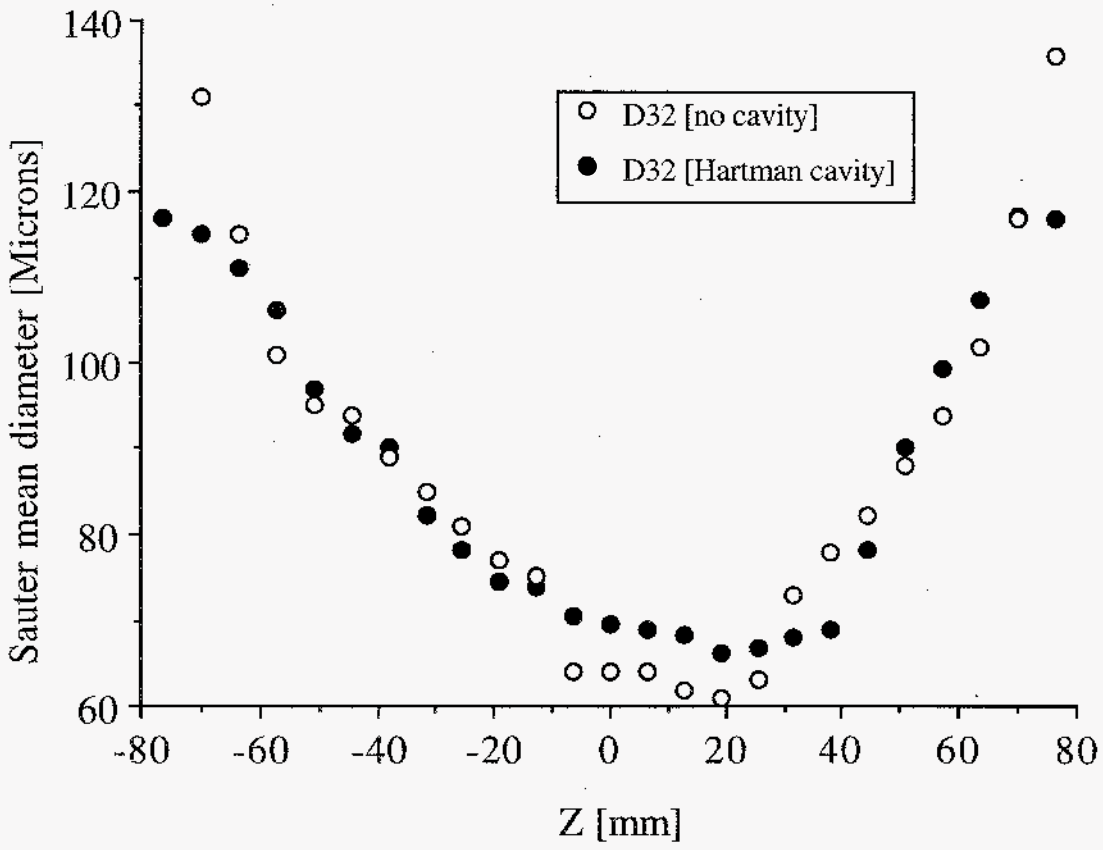

Fig. 18 Effect of Hartman Cavity on SMD Profile at x = 254 mm, y = 0 mm, P_o = 239.26 kPa, m_l = 26.67 g/s.

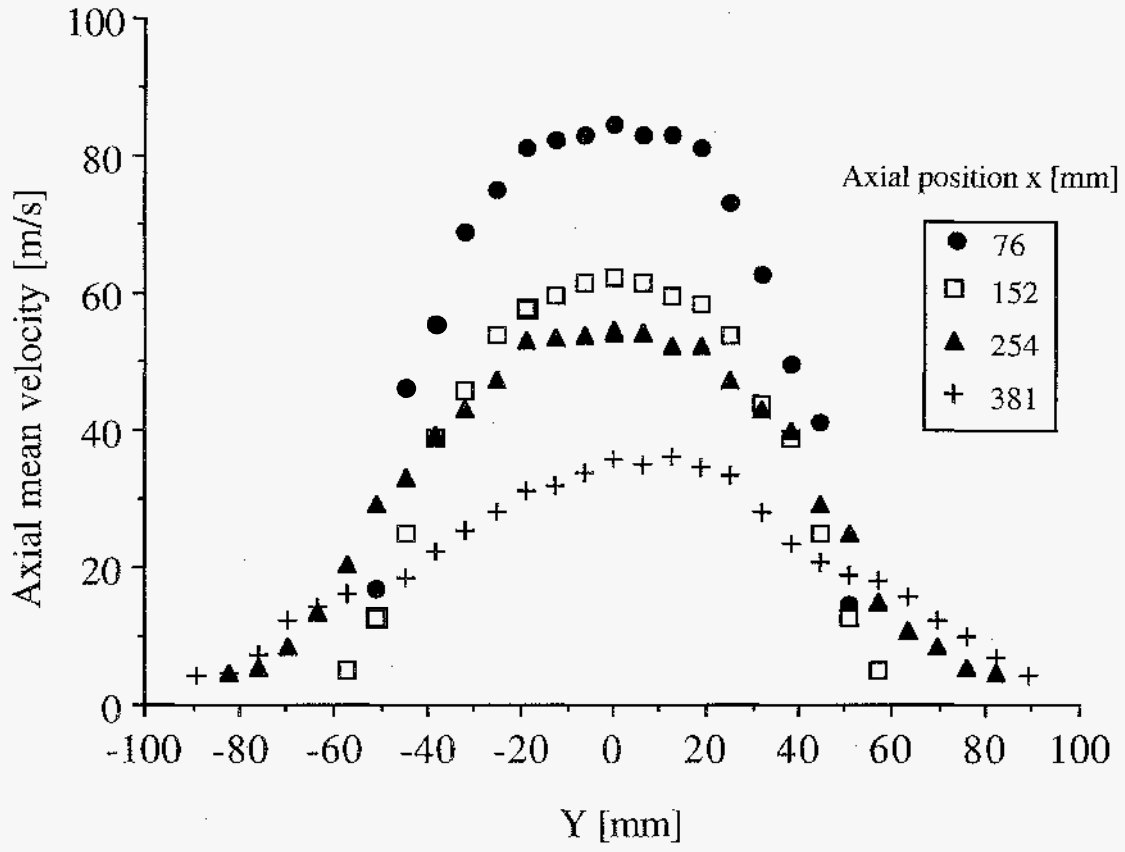

Fig. 19 Y-Direction Air Velocity Profile Development (P_o = 239.26 kPa, m_j = 0 g/s).

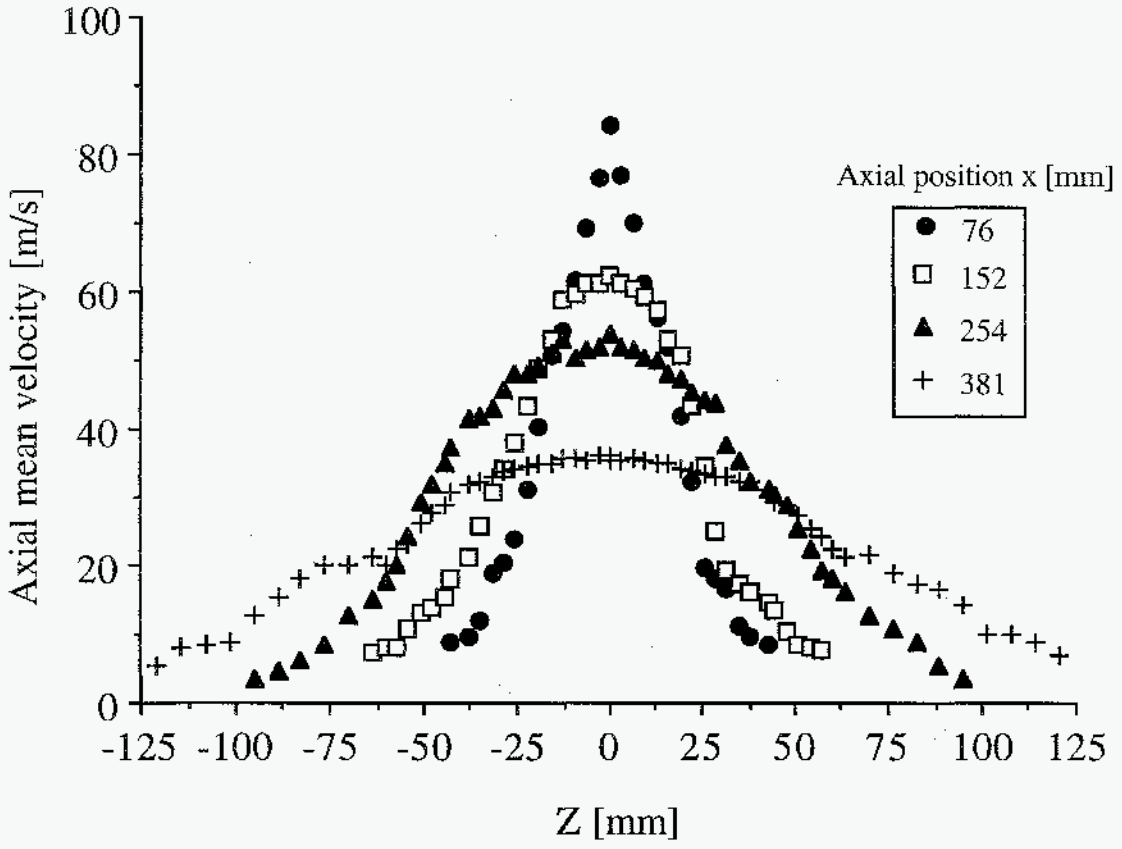

Fig. 20 Z-Direction Air Velocity Profile Development (P_o = 239.26 kPa, m_l = 0 g/s).

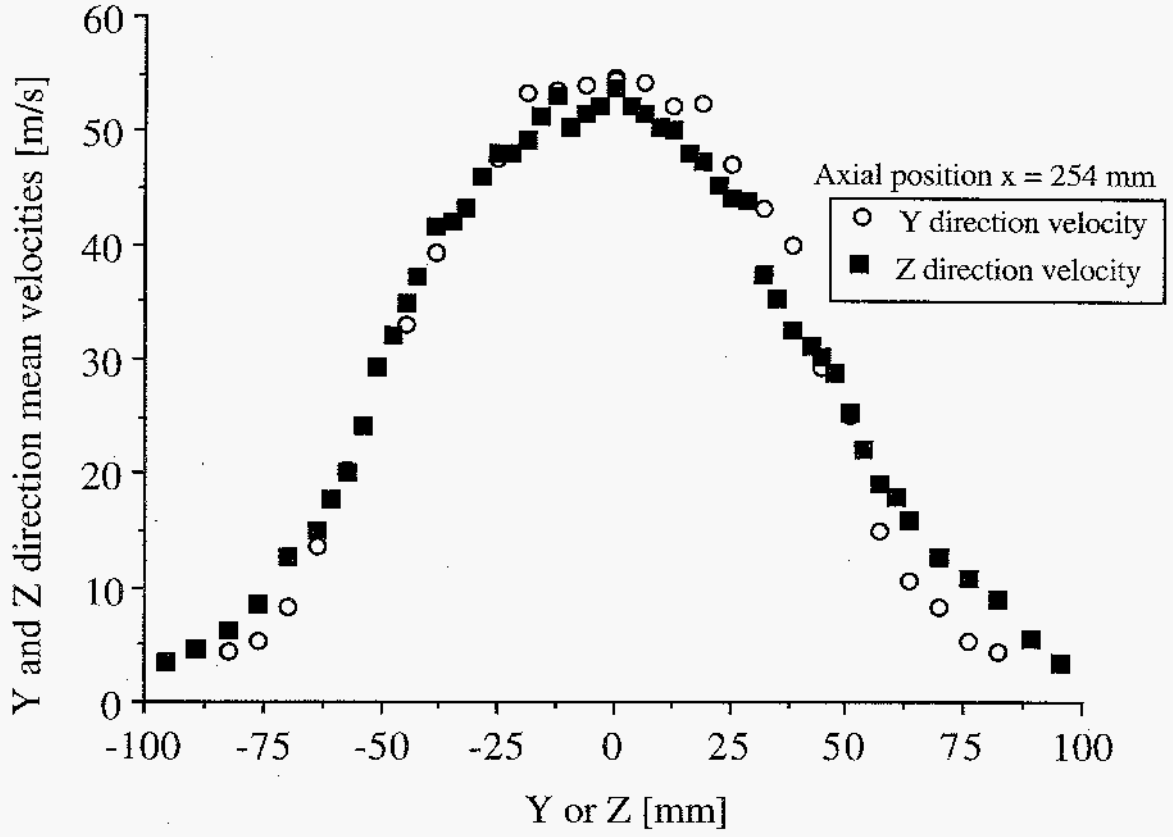

Fig. 21 Y and Z-Direction Air Velocity Profiles at x = 254 mm (P_o = 239.26 kPa, m_l = 0 g/s).

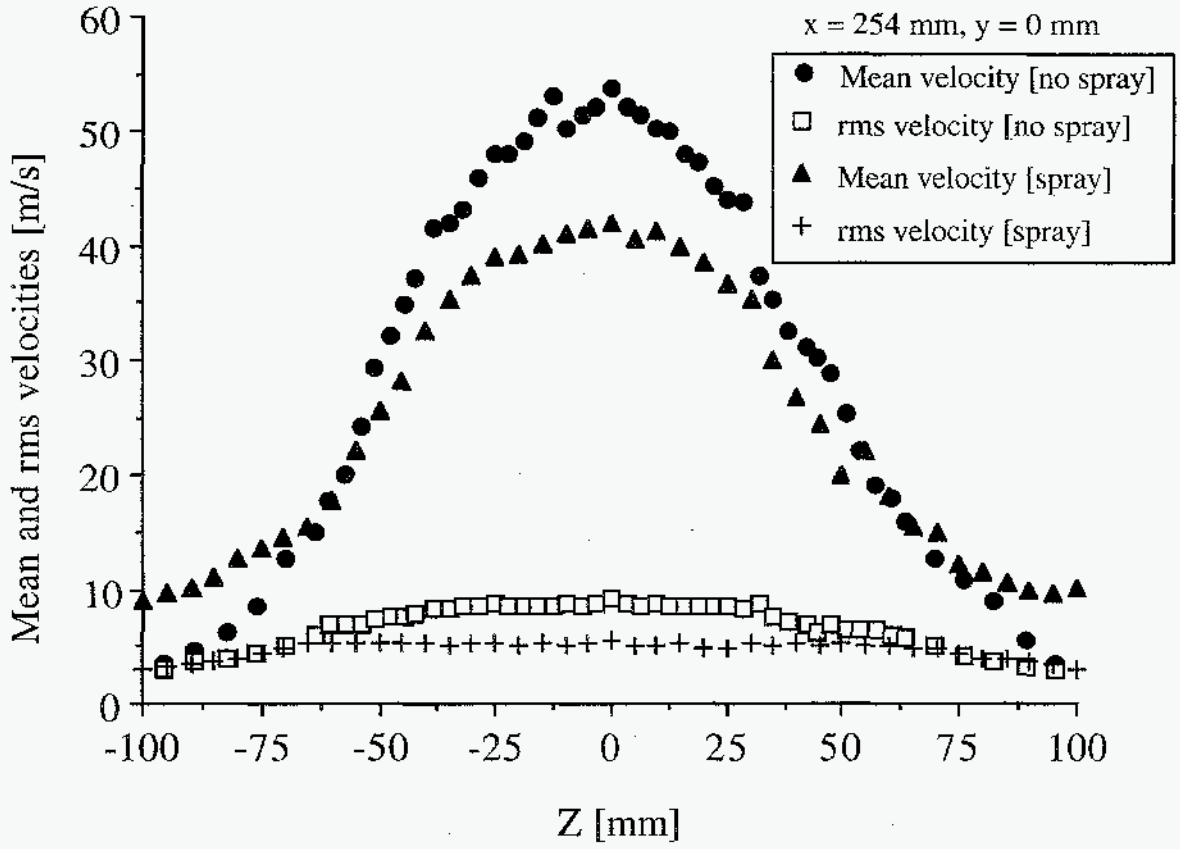

Fig. 22 Z-Direction Mean and RMS Velocity of air flow and spray at x = 254 mm, y = 0 mm (P_o = 239.26 kPa).

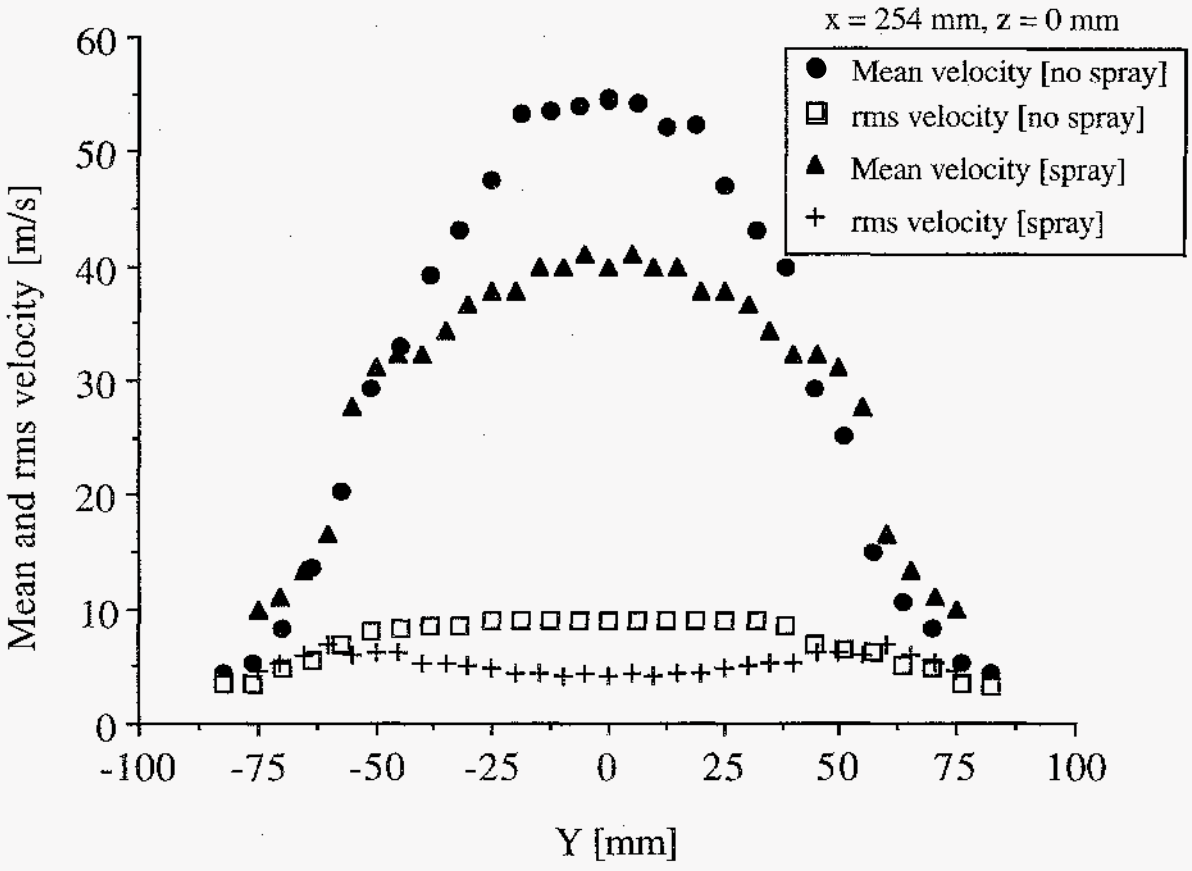

Fig. 23 Y-Direction Mean and RMS Velocity of air flow and spray at x = 254 mm, z = 0 mm (P_o = 239.26 kPa).

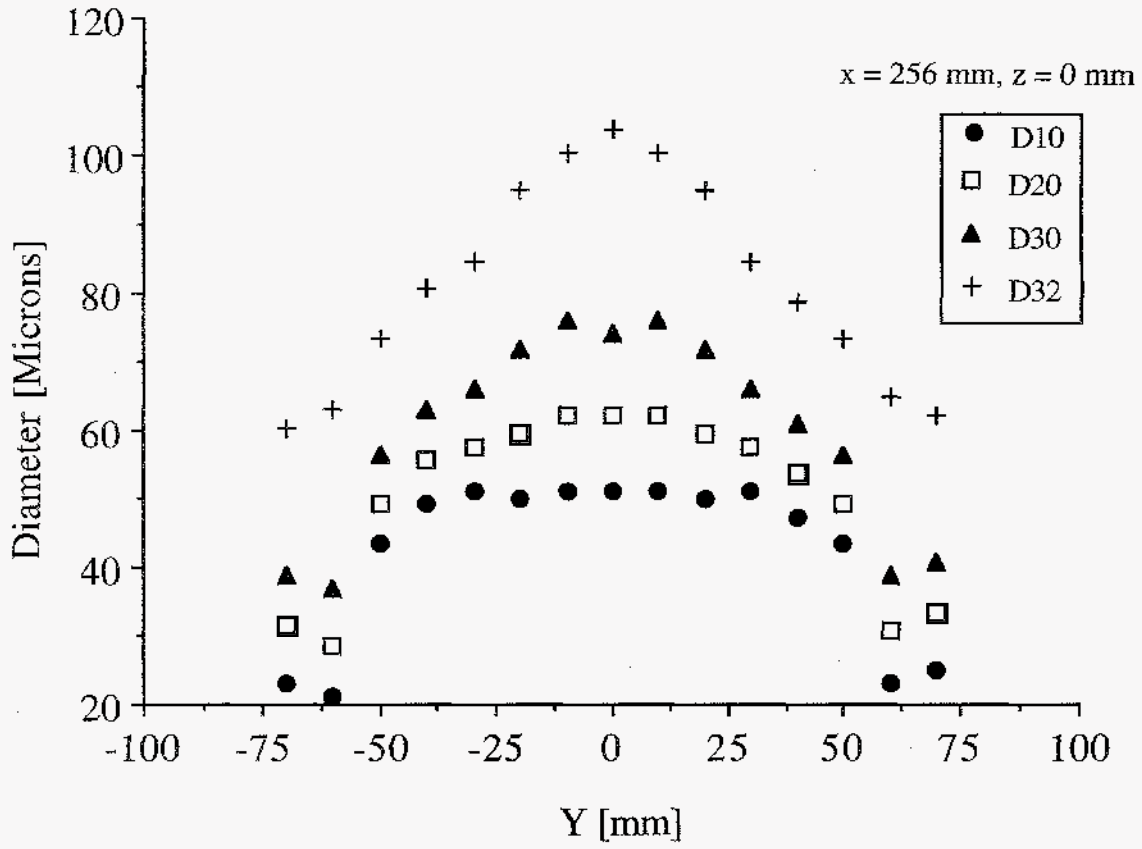

Fig. 24 Y-Direction Spray Size Distribution at x = 254 mm, z = 0 mm (P_o = 239.26 kPa).

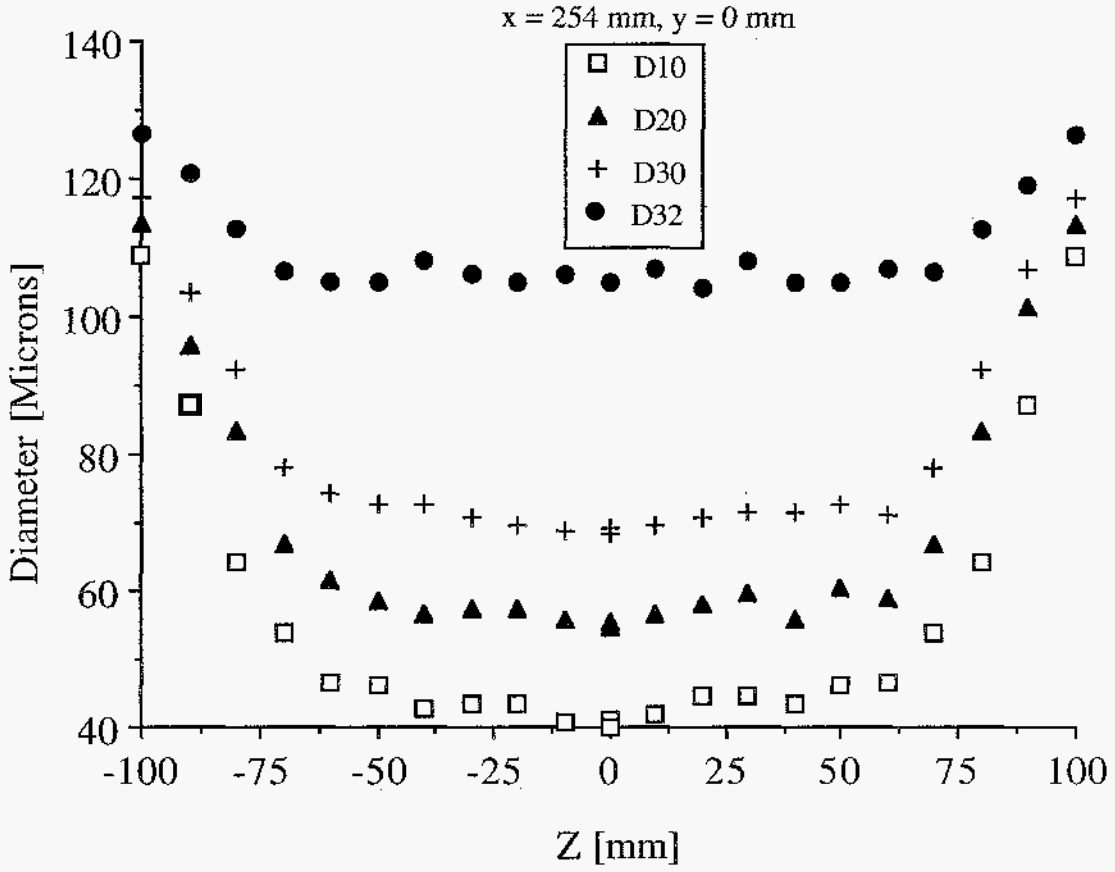

Fig. 25 Z-Direction Spray Size Distribution at x = 254 mm, y = 0 mm (P_o = 239.26 kPa)

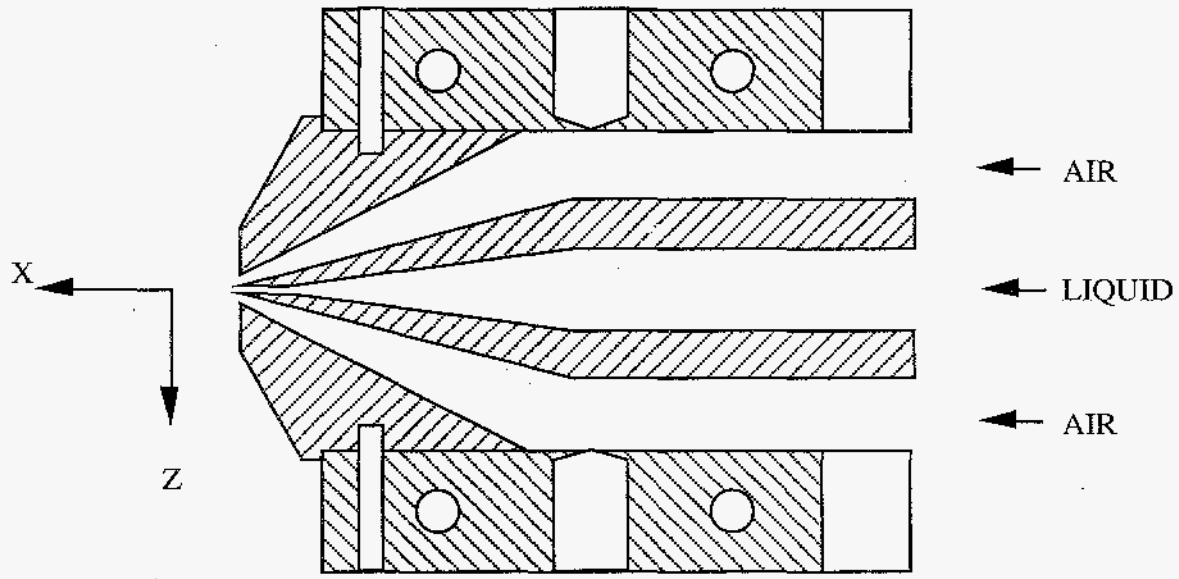

Fig. 26 The Two-Dimensional Airblast Atomizer

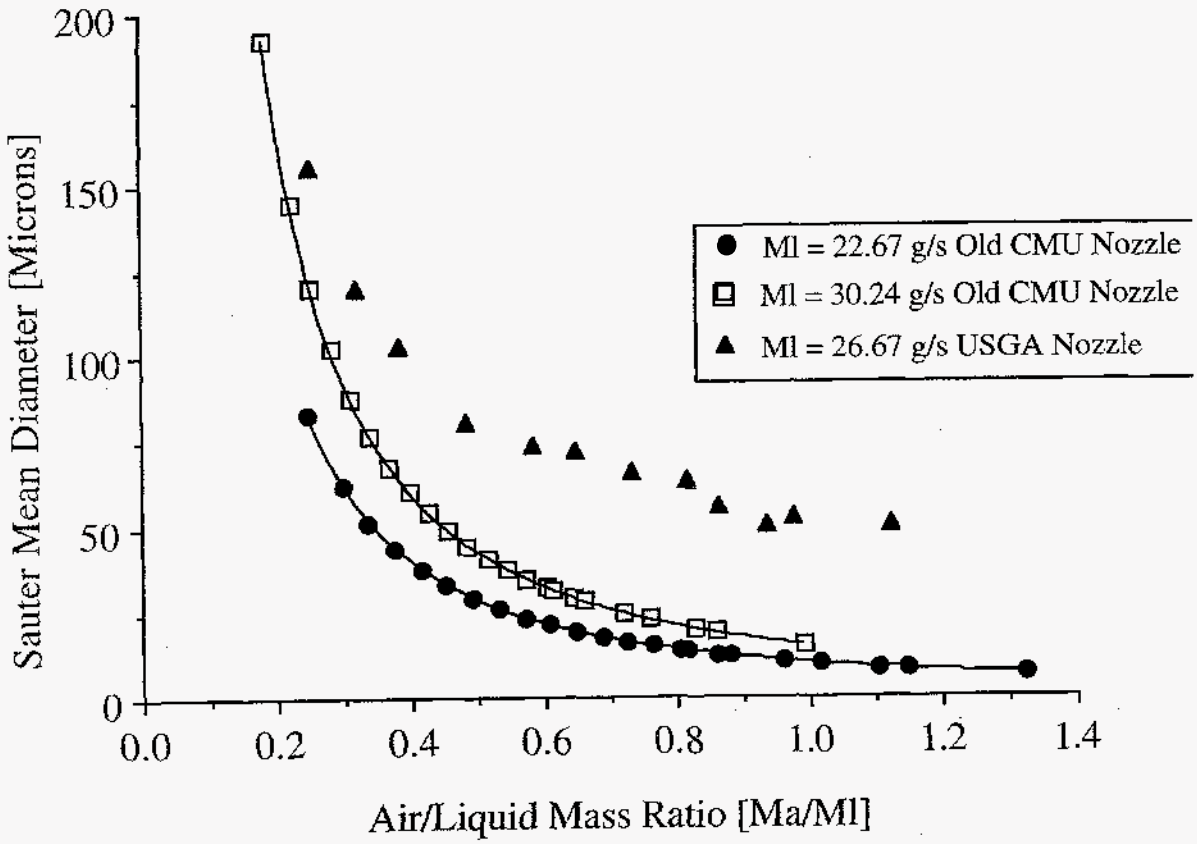

Fig. 27 Comparison Between the USGA Nozzle Performance and the CMU 2-D Nozzle Performance.